

1 **Dynamics-based estimates of decline trend with fine temporal variations in China's**
2 **PM_{2.5} emissions**

3
4 **Zhen Peng^{1†}, Lili Lei^{1,2†}, Zhe-Min Tan^{1,2*}, Meigen Zhang^{3*}, Aijun Ding¹ and Xingxia Kou⁴**

5 ¹School of Atmospheric Sciences, Nanjing University, Nanjing 210093, China

6 ²Key Laboratory of Mesoscale Severe Weather, Ministry of Education, Nanjing University,
7 Nanjing 210093, China

8 ³State Key Laboratory of Atmospheric Boundary Layer Physics and Atmospheric Chemistry,
9 Institute of Atmospheric Physics, Chinese Academy of Sciences, Beijing 100029, China

10 ⁴Institute of Urban Meteorology, China Meteorological Administration, Beijing 100089, China

11
12 Corresponding author: Zhe-Min Tan (zmtan@nju.edu.cn) and Meigen Zhang
13 (mgzhang@mail.iap.ac.cn)

14
15 **Abstract**

16 Timely, continuous, and dynamics-based estimates of PM_{2.5} emissions with a high temporal
17 resolution can be objectively and optimally obtained by assimilating observed surface PM_{2.5}
18 concentrations using flow-dependent error statistics. The annual dynamics-based estimates of
19 PM_{2.5} emission averaged over mainland China for years 2016-2020 without biomass burning
20 emissions are 7.66, 7.40, 7.02, 6.62 and 6.38 Tg, respectively, which are very closed to the values
21 of MEIC. Annual PM_{2.5} emissions in China have consistently decreased of approximately 3% to
22 5% from 2017 to 2020. Significant PM_{2.5} emission reductions occurred frequently in regions with
23 large PM_{2.5} emissions. COVID-19 could cause a significant reduction of PM_{2.5} emissions in the
24 north China plain and northeast of China in 2020. The magnitudes of PM_{2.5} emissions were greater
25 in the winter than in the summer. PM_{2.5} emissions show an obvious diurnal variation that varies
26 significantly with the season and urban population. Compared to the diurnal variations of PM_{2.5}

27 emission fractions estimated based on diurnal variation profiles from US and EU, the estimated
28 PM_{2.5} emission fractions are 1.25% larger during the evening, the morning peak is 0.57% smaller
29 in winter and 1.05% larger in summer, and the evening peak is 0.83% smaller. Improved
30 representations of PM_{2.5} emissions across time scales can benefit emission inventory, regulation
31 policy and emission trading schemes, particularly for especially for high temporal resolution air
32 quality forecasting and policy response to severe haze pollutions or rare human events with
33 significant socioeconomic impacts.

34

35 **1. Introduction**

36 Anthropogenic emissions have imposed essential influences on the earth system, from
37 hourly air quality and human health to long-time climate and environment. To reduce
38 anthropogenic emissions, the Chinese government has enforced the Clean Air Action (2013) since
39 2013. Studies to date that evaluated the emission controls and understood the climate responses
40 from emission reductions often have used either a fixed meteorology with emission changes or
41 *vice versa* (Li et al., 2019a; Li et al., 2021, Zhai et al., 2021). Estimated emissions from empirical
42 extrapolation were commonly applied to analyze the meteorological-chemical mechanisms and
43 associated social-economic impacts from occasional events like the 2015 China Victory Day
44 Parade and Coronavirus Disease 2019 (COVID-19) pandemic (Wang et al., 2017; Liu et al., 2020;
45 Huang et al., 2020; Zhu et al., 2021). But to better understand both long-term and short-term
46 influences from emission changes, the continuous, up-to-date, and high temporal-/spatial-
47 resolution emission estimates with coherent interactions of meteorology and emission changes are
48 needed.

49 The complex contributions from energy production, industrial processes, transportation,
50 and residential consumptions have imposed great challenges to accurately estimate the emissions.
51 The emission inventories created by the traditional bottom-up techniques were typically outdated
52 from the present day due to the lack of accurate and timely statistics, and often with coarse
53 temporal resolutions from monthly to annual (Zhang et al., 2009; Li et al., 2014; Janssens-
54 Maenhout et al., 2015; Zheng et al., 2018). Alternatively, update-to-date emission estimates with
55 high temporal-spatial resolutions could be provided by top-down techniques (Miyazaki et al.,
56 2017), but most emissions estimated by top-down techniques were intermittent and analyzed at

57 monthly scale or longer longer (Zhang et al., 2016; Jiang et al., 2017; Qu et al., 2017; Cao et al.,
58 2018; Müller et al., 2018; Chen et al., 2019; Li et al., 2019b; Miyazaki et al., 2020). Moreover,
59 emissions updated by the top-down techniques based on satellite observations could be insufficient
60 to capture realistic near-surface characteristics (Li et al., 2019b; Liu et al., 2011; Choi et al., 2020).

61 Given the development of observation networks and advanced data assimilation strategies,
62 timely and dynamics-based emission estimates with high temporal resolution can be achieved by
63 harmonically constraining the atmospheric-chemical model with dense observations of trace gas
64 compounds through an optimal assimilation methodology. The ensemble Kaman smoother (EnKS)
65 (Whitaker et al., 2002; Peters et al., 2007; Peng et al., 2015), as a four-dimensional (4D)
66 assimilation algorithm, makes use of chemical observations from past to future to provide an
67 optimal estimate of source emissions, and it can capture the “error of the day” and construct fine
68 emission characteristics with high temporal-spatial resolutions by using short-term ensemble
69 forecasts (Kalnay, 2002). Since 2013, the fine particulate matter pollution (PM_{2.5}, particles smaller
70 than 2.5 μm in diameter) as the most urgent threat to public health has been persistently decreased,
71 and ground-based observations of PM_{2.5} have been progressively increased (Huang et al., 2018).
72 Thus by harmonically assimilating dense surface PM_{2.5} observations into an atmospheric-chemical
73 model through an EnKS, hourly estimates of PM_{2.5} emission that were continuously cycled for
74 years 2016-2020 are presented in this study.

75 The timely estimated emissions can provide guidance for emission inventories that usually
76 have time lags and emission trading schemes that often require up-to-date source emissions. Based
77 on the dynamics-based estimated emissions with harmonic combination of the model and
78 observations, better evaluation of the emission controls and more comprehensive understanding of
79 the consequent climate responses can be obtained. The high temporal-resolution estimated
80 emissions can reveal features of emissions that are absent from the traditional ones with coarse
81 temporal resolutions. Moreover, the timely and dynamics-based emission estimates with high
82 temporal resolution are essential for regional air quality modeling, especially for the occurrence of
83 severe haze pollutions associated with timely evaluation for the impact on public health (Attri et
84 al., 2001; Wang et al., 2014; Ji et al., 2018; Wang et al., 2020; Liu et al., 2021) and events that
85 lead to large changes of emissions and significant socioeconomic impacts such as the COVID-19
86 pandemic (Huang et al., 2020; Le et al., 2020).

87 2. Data assimilation and experimental design

88 The estimate of PM_{2.5} emission can be successfully constrained by the PM_{2.5} concentration
89 observations through an ensemble Kalman filter (EnKF; Peng et al., 2017, 2018, 2020). For a
90 retrospective ‘reanalysis’ mode here, all available PM_{2.5} concentration observations, including
91 those data collected after the analysis time, can be used. Thus a EnKS, a direct generalization of
92 the EnKF, is applied to incorporate PM_{2.5} concentration observations both before and after the
93 analysis time, aiming to provide an optimal estimate of the PM_{2.5} emission. In simple words, The
94 emissions are updated by current and future observations though EnKS, while the concentrations
95 are updated by current observations though EnKF. Detailed procedures of the EnKS are described
96 in section 2.1.

97 2.1 An ensemble Kalman smoother to update the source emission

98 The ensemble priors of source emissions \mathbf{e}^f is created by multiplying a scaling factor λ^f
99 to the prescribed emission \mathbf{e}^p (Peng et al., 2017, 2018, 2020), where the superscript f denotes priors.
100 Given a time-invariant \mathbf{e}^p , the update of \mathbf{e}^f is equivalent to the update of λ^f . Due to a time lag,
101 the prior scaling factor at time $t-1$ (λ_{t-1}^f) is updated by chemical observations at time t (\mathbf{y}_t^c). At time
102 $t-1$, the prior scaling factor for the i^{th} member is written as

$$103 \lambda_{i,t-1}^f = \frac{1}{M} \left[\left(\beta \frac{\mathbf{c}_{i,t-1}^f}{\bar{\mathbf{c}}_{t-1}^f} + 1 - \beta \right) + \sum_{j=t-M}^{t-2} \lambda_{i,j|j+1:t-1}^a \right]. \quad (1)$$

104 The first term is the concentration ratio given by the prior of the chemical fields ($\mathbf{c}_{i,t-1}^f$) normalized
105 by the ensemble mean ($\bar{\mathbf{c}}_{t-1}^f$), where β is an inflation factor used to compensate the insufficient
106 ensemble spread (Peng et al., 2017). Through using the concentration ratio, each ensemble member
107 of the source emissions naturally has the spatial correlations given by the chemical fields. The
108 second term is the mean of the posterior scaling factors at previous assimilation cycles, where the
109 superscript a denotes posteriors, M is the length of smoothing, and the subscript $j+1:t-1$ indicates
110 that the scaling factor at time j is updated by future observations from $j+1$ to $t-1$. The assimilation
111 of future observations will be described below.

112 The ensemble square-root filter (EnSRF) (Peng et al., 2017) is used to update λ_{t-1}^f by
 113 assimilating \mathbf{y}_t^c . For the scaling factor at time $t-1$, posterior ensemble mean is given by

$$114 \quad \bar{\lambda}_{t-1}^a = \bar{\lambda}_{t-1}^f + \rho \circ \mathbf{P}_{t-1,t}^{ec} \mathbf{H}_t^{cT} \left(\mathbf{H}_t^c \mathbf{P}_t^c \mathbf{H}_t^{cT} + \mathbf{R}_t^c \right)^{-1} \left(\mathbf{y}_t^c - H_t^c \bar{\mathbf{c}}_t^f \right), \quad (2)$$

115 and posterior ensemble perturbations are given by

$$116 \quad \lambda_{i,t-1}^a = \lambda_{i,t-1}^f - \rho \circ \mathbf{P}_{t-1,t}^{ec} \mathbf{H}_t^{cT} \left[\left(\sqrt{\mathbf{H}_t^c \mathbf{P}_t^c \mathbf{H}_t^{cT} + \mathbf{R}_t^c} \right)^{-1} \right]^T \left[\sqrt{\left(\mathbf{H}_t^c \mathbf{P}_t^c \mathbf{H}_t^{cT} + \mathbf{R}_t^c \right) + \sqrt{\mathbf{R}_t^c}} \right]^{-1} \mathbf{H}_t^c \lambda_{i,t-1}^f, \quad (3)$$

118 where $\mathbf{P}_{t-1,t}^{ec}$ denotes the background error covariance matrix of λ_{t-1}^f and \mathbf{c}_t^f , \mathbf{P}_t^c indicates the
 119 background error covariance matrix of \mathbf{c}_t^f , H_t^c , \mathbf{H}_t^c and \mathbf{R}_t^c are the observation forward operator,
 120 Jacobian matrix and observation error covariance matrix of the chemical fields at time t , ρ is the
 121 localization matrix and \circ denotes the Schur (elementwise) product.

122 By applying the ensemble Kalman smoother (EnKS) (Whitaker et al., 2002; Peters et al.,
 123 2007), the chemical observation \mathbf{y}_t^c is also assimilated to update the posterior scaling factor at
 124 previous assimilation cycles $j (j = t - K, \dots, t - 2)$. After assimilating the future chemical
 125 observation at time t , posterior ensemble mean of the scaling factor at j is given by

$$126 \quad \bar{\lambda}_{j|j+1:t}^a = \bar{\lambda}_{j|j+1:t-1}^a + \rho \circ \mathbf{P}_{j|j+1:t-1,t}^{ec} \mathbf{H}_t^{cT} \left(\mathbf{H}_t^c \mathbf{P}_t^c \mathbf{H}_t^{cT} + \mathbf{R}_t^c \right)^{-1} \left(\mathbf{y}_t^c - H_t^c \bar{\mathbf{c}}_t^f \right), \quad (4)$$

127 and posterior ensemble perturbations are given by

$$128 \quad \lambda_{i,j|j+1:t}^a = \lambda_{i,j|j+1:t-1}^a - \rho \circ \mathbf{P}_{j|j+1:t-1,t}^{ec} \mathbf{H}_t^{cT} \left[\left(\sqrt{\mathbf{H}_t^c \mathbf{P}_t^c \mathbf{H}_t^{cT} + \mathbf{R}_t^c} \right)^{-1} \right]^T \left[\sqrt{\left(\mathbf{H}_t^c \mathbf{P}_t^c \mathbf{H}_t^{cT} + \mathbf{R}_t^c \right) + \sqrt{\mathbf{R}_t^c}} \right]^{-1} \mathbf{H}_t^c \lambda_{i,t-1}^f, \quad (5)$$

129 where $\mathbf{P}_{j|j+1:t-1,t}^{ec}$ denotes the background error covariance matrix of $\lambda_{j|j+1:t-1}^a$ and \mathbf{c}_t^f . After (2)-(5),
 130 the updated $\lambda_{j|j+1:t}^a, j (j = t - M + 1, \dots, t - 1)$ will be used to construct the prior scaling factor at next
 131 time $t+1$ (1).

132 As a Monte Carlo approach, the EnKS uses the forecast-analysis error covariances based
133 on ensemble forecasts / analyses to compute the Kalman gain matrix with time lags, to incorporate
134 observations from the past to the future. The first iteration of EnKS is equivalent to EnKF that
135 assimilates observations up to the analysis time. The following iterations of EnKS assimilate
136 observations in the future to update the state at the analysis time. The hourly forecasts of PM_{2.5}
137 concentration from the cycling assimilation experiment matched the independent observed
138 quantities (Figure 1). Therefore, the ability of EnKS to retrieve the source emissions has been
139 demonstrated. Previous studies also showed that simulations forced by the posterior emissions
140 could produce improved forecasts for PM_{2.5}, SO₂, and NO₂ than those with a priori emissions
141 (Peng et al., 2020).

142 **2.2 WRF-Chem model, observations and emissions**

143 To simulate the transport of aerosol and chemical species, the WRF-Chem model version
144 3.6.1 (Grell et al., 2005) that has the meteorological and chemical components fully coupled is
145 used. The model parameterization schemes follow Peng et al. (2017). Figure 2 shows the model
146 domain that covers most east Asia regions. Horizontal grid spacing is 45 km with 57 vertical levels
147 and model top at 10 hPa.

148 Experiments are conducted for each year from 2016 to 2020 separately. The 6-h
149 meteorological observations, including all in-situ observations and cloud motion vectors from the
150 National Centers for Environmental Prediction (NCEP) Global Data Assimilation System (GDAS;
151 http://www.emc.ncep.noaa.gov/mmb/data_processing/prepbufn.doc/table_2.htm), are assimilated
152 every 6 h. The hourly observed chemical quantities, which contain PM₁₀, PM_{2.5}, SO₂, NO₂, O₃,
153 and CO from the Ministry of Ecology and Environment of China (<https://aqicn.org/map/china/cn/>),
154 are assimilated every hour. Figure 2 shows the assimilated chemical observation network, which
155 has 560 randomly chosen stations from 1576 stations in total. The thinning of observations is
156 applied to avoid correlated errors of observations. The spatial autocorrelation of the thinning of
157 observations is close to the original observations (Peng et al., 2017). The observation priors are
158 computed by the “observer” portion of the Grid-point Statistical Interpolation system (GSI) (Kleist
159 et al., 2009).

160 The hourly and time-invariantly prescribed anthropogenic emissions are obtained from the
161 EDGAR-HTAP (Emission Database for Global Atmospheric Research for Hemispheric Transport

162 of Air Pollution v2.2) v2.2 inventory (Janssens-Maenhout et al., 2015), in which the Chinese
163 emissions are derived from MEIC in 2010 (Lei et al., 2011; Li et al., 2014). Natural emissions,
164 including the biogenic (Guenther et al., 1995), dust (Ginoux et al., 2001), dimethyl sulfide and sea
165 salt emissions (Chin et al., 2000), are computed online.

166 **2.3 Assimilation and ensemble configurations**

167 The $PM_{2.5}$ emission directly gives the primary $PM_{2.5}$, and then the primary $PM_{2.5}$ along
168 with other precursor emissions could contribute to the secondary $PM_{2.5}$. The observations of $PM_{2.5}$
169 concentrations that contain both primary and secondary $PM_{2.5}$, are used to constrain the $PM_{2.5}$
170 emission through data assimilation. Thus the correlations between the concentration observations
171 and source emissions might be contaminated by the secondary $PM_{2.5}$. Since the secondary
172 formation process can be captured by the WRF-Chem model, the impact of the secondary $PM_{2.5}$
173 is indirectly considered. The detailed updated state variables with the according observations
174 follow Peng et al. (2018). The concentrations and emissions of $PM_{2.5}$, NH_3 , and $PM_{2.5}$ precursors
175 that have observations (SO_2 and NO), are updated by the observed quantities, respectively, but the
176 VOC that are also $PM_{2.5}$ precursors are not updated due to the lack of direct and limited
177 observations.. One possible way to untangle the impact of secondary $PM_{2.5}$ on the estimates of
178 $PM_{2.5}$ emission is to jointly estimate the source emission, primary and secondary $PM_{2.5}$ given the
179 concentration observations.

180 The National Oceanic and Atmospheric Administration (NOAA) operational EnKF system
181 (https://dtcenter.ucar.edu/com-GSI/users/docs/users_guide/GSIUserGuide_v3.7.pdf), which is an
182 EnSRF and modified with the EnKS feature, is used to assimilate the observations. Ensemble size
183 is set to 50. To combat the sampling error resulted from a limited ensemble size, covariance
184 localization and inflation are applied. The Gaspari and Cohn (GC) (1999) function with a length
185 scale of 675 km is used to localize the impact of observations and mitigate the spurious error
186 correlations between observations and state variables. The constant multiplicative posterior
187 inflation (Whitaker and Hamill 2012) with coefficients 1.12 for all meteorological and chemical
188 variables is applied to enlarge the ensemble spread. The inflation β for advancing the scale factor
189 is 1.2. The smoothing length M for source emissions is 4, and the EnKS lagged length K is 6. The
190 larger the K value, the more future observations are assimilated to constrain the current emission
191 estimate. But the sample estimated temporal correlations could be contaminated by sampling errors

192 and model errors, especially with increased lagged times. Thus, there is a tradeoff between the
193 amount of future observations and accuracy of sample estimated temporal correlations. The choice
194 of $K (=6)$ is determined by sensitivity experiments.

195 At 0000 UTC 26 December of previous year, ensemble initial conditions (ICs) of the
196 meteorological fields are generated by adding random perturbations that sample the static
197 background error covariances (Barker et al., 2012) on the NCEP FNL (Final) analyses (Torn et al.,
198 2006). Ensemble ICs of the chemical fields are 0, and source emissions of each ensemble member
199 are adopted from the EDGAR-HTAP v2.2 inventory with random perturbations of mean 0 and
200 variances of 10% of the emission values. Hourly ensemble lateral boundary conditions (LBCs) are
201 generated using the same fixed-covariance perturbation technique as the ensemble ICs. After 6-d
202 spin up, ensemble data assimilation experiments start cycling for each year.

203 **3. PM_{2.5} emission for years 2016-2020**

204 Starting from the time-invariant source emission PR2010 (Janssens-Maenhout et al., 2015),
205 the dynamics-based estimates of the PM_{2.5} emissions are obtained, which include both the
206 contributions of the anthropogenic and biomass burning emissions. The mean annual PM_{2.5}
207 emissions from biomass burning in China (2003~2017) was 0.51 Tg (Yin et al., 2019). The annual
208 dynamics-based estimates of PM_{2.5} emission (DEPE) averaged over mainland China for years
209 2016-2020 without biomass burning emissions are 7.66, 7.40, 7.02, 6.62 and 6.38 Tg, respectively.
210 The values from the Multi-resolution Emission Inventory (MEIC; Zheng et al., 2018) that does not
211 consider the contributions of biomass burning emissions, are 8.10, 7.60, 6.70, 6.38 and 6.04 Tg,
212 respectively. Thus the annual DEPE are very closed to the values of MEIC. From year 2017 to
213 2020, the estimated annual PM_{2.5} emissions are reduced 3.4%, 8.4%, 13.6% and 16.7%
214 respectively compared to that of year 2016. There has been 3%-5% persistent reduction of annual
215 PM_{2.5} emission from year 2017 to 2020, which demonstrates the effectiveness of China's Clean
216 Air Action (2013) implemented since 2013 and China Blue Sky Defense War Plan (2018) enforced
217 since 2018 with strengthened industrial emission standards, phased out outdated industrial
218 capacities, promoted clean fuels in residential sector and so on (Zhang et al., 2019).

219 The monthly DEPE show reduction of PM_{2.5} emission nearly in each month from years
220 2016 to 2020 (Figure 3a), which further demonstrates the effectiveness of China's national plan.
221 Compared to year 2016, both the reduction amount and reduction ratio of PM_{2.5} emission are more

222 prominent for February, March, June-September, and November than the other months (Figure3b).
223 Given larger magnitudes of $PM_{2.5}$ emission in winter than in summer, emission controls with a
224 focus from October to May should be considered in the design of future clean air actions in China,
225 since total $PM_{2.5}$ emission during this period accounts for approximate 75% annual amount. Spatial
226 distributions of the changes of $PM_{2.5}$ emission from year 2017 to 2020 compared to year 2016
227 show significant decreases occurred at Beijing-Tianjin-Hebei region (BTH), Yangtze River Delta
228 region (YRD), Pearl River Delta region (PRD) and Sichuan-Chongqing Region (SCR), especially
229 for years 2019-2020 (Figure 4). From year 2016 to 2020, BTH, YRD and SRC have larger
230 reductions of $PM_{2.5}$ emission than PRD, but SCR has larger reduction ratio compared to year 2016
231 than BTH and YRD (Figure 5). Therefore, BTH and YRD have more potentials for $PM_{2.5}$ emission
232 controls than PRD and SCR, which can give a guidance for future clean air actions. More
233 specifically, most provinces have $PM_{2.5}$ emission reduction from year 2016 to 2020, and the
234 reduction ratios generally increase from year 2017 to 2020 (Table 1), which confirms continuous
235 and effective emission controls from Clean Air Action to Blue Sky Defense War Plan in China.
236 The monthly DEPE also demonstrates the effectiveness of strict implementations of emission
237 reduction policies in China, such as the coal ban for residential heating since the 2017-2018 winter.
238 There was a sharp change of $PM_{2.5}$ emission, from increase in 2017 to decrease in 2018. As shown
239 by Figure 6, spatial distributions of the changes of $PM_{2.5}$ emissions in December compared to
240 November in 2017 show obvious increases in most China. However, the changes in 2018 show
241 significant decreases in areas of Beijing, Tianjin, Hebei, Shanxi, Henan and Anhui provinces due
242 to the implementation of the coal ban.

243 Despite the trend in $PM_{2.5}$ emissions from year 2016 to 2020, the DEPE of year 2016 has
244 similar monthly distributions to MEIC2016-2020 in general (Figure 3a). MEIC has a “Pan-shape”
245 monthly distribution with nearly time-invariant $PM_{2.5}$ emissions from April to October. This
246 seasonal dependence of emissions is mainly contributed by the variations of residential energy use,
247 which are empirically dependent on coarse monthly mean temperature intervals and thus cannot
248 reflect the realistic monthly variations (Streets et al., 2003; Li et al., 2017). The centralized heating
249 system in North China has a fixed date of turning-on and turning-off during each heating season.
250 Therefore, a sudden raise of emissions from October to November and a sudden drop of emissions
251 from March to April are shown. But the turning-on and turning-off date are variable in different
252 regions, which imposes a smoothing impact on the emissions. However, the DEPE yet shows a

253 “V-shape” monthly distribution, with the minimum occurring in August. The estimated $PM_{2.5}$
254 emission is 11.8% higher than MEIC2016 in April but 12.1% lower than MEIC2016 in August,
255 and these different monthly distributions can influence the consequent climate responses including
256 the radiative forcing and energy budget (Yang et al., 2020) and also impact the health issues (Liu
257 et al., 2018). Moreover, monthly fractions of the DEPE are consistent cross years (Figure 3c). The
258 absence of interannual variations of monthly $PM_{2.5}$ emission fraction provides basis for previous
259 studies that follow the same monthly changes of source emissions from different years (Zhang et
260 al., 2009; Zheng et al., 2020, 2021). Monthly allocations of $PM_{2.5}$ emission can be directly and
261 objectively obtained given an estimated total annual amount based on the estimated monthly
262 fractions of DEPE, which is valuable for emission inventory, air quality simulation, and potentially
263 applications for future scenarios due to more accurate month fractions of DEPE. Since the hourly
264 priors of $PM_{2.5}$ concentrations from the cycling assimilation for optimally estimating $PM_{2.5}$
265 emission fit to the observed $PM_{2.5}$ quantities (Figure 1), the monthly DEPE provides more realistic
266 monthly fluctuations than the empirical estimate.

267 **4. Diurnal variations of $PM_{2.5}$ emission**

268 The DEPE with high temporal-resolution given the time-invariant prior PR2010 can reveal
269 features that are unable to represent in the commonly used emission estimates. Although the prior
270 PR2010 has no diurnal variations, hourly posteriors of $PM_{2.5}$ emission provide the first objectively
271 estimated diurnal variations for different seasons for years 2016-2020. However, these estimated
272 diurnal variations include the contributions of the time-varying boundary layer. An observing
273 system simulation experiment (OSSE) is performed to investigate the effects of the boundary layer.
274 Details of this OSSE are presented in Appendix. The results indicate that the magnitude of
275 posterior $PM_{2.5}$ emission from the OSSE is closer to the true emission than the prior. Since we
276 have hourly assimilated observations to simultaneously update the chemical concentrations and
277 source emissions, the impacts of time-varying boundary layer on the posterior $PM_{2.5}$ emissions are
278 limited (Figures S1). A little larger estimated $PM_{2.5}$ emission fractions occurred in the morning
279 and smaller estimated $PM_{2.5}$ emission fractions occurred in the afternoon, comparing to the time-
280 invariant true emission. Nevertheless, the influences of time-varying boundary layer are still
281 important to $PM_{2.5}$ emission estimates. To statistically present the diurnal variations, the fractions
282 of hourly $PM_{2.5}$ emissions divided by the daily amount are averaged over different years and

283 regions after excluding the impacts of time-varying boundary layer (Figures 7 and 8, and Table 2).
284 The diurnal variations of PM_{2.5} emission are critical for understanding the mechanisms of PM_{2.5}
285 formation and evolution and are also essential for PM_{2.5} simulation and forecast.

286 Five-year mean diurnal variations of the estimated PM_{2.5} emission fraction for mainland
287 China show that despite the monthly variations of PM_{2.5} emission, the diurnal-variation fractions
288 for November, December, January and February are similar, while those for June, July and August
289 are similar (Figure 7a). There are stronger diurnal variations of PM_{2.5} emission in summer than in
290 winter, which are represented by larger PM_{2.5} emission fractions during morning and less PM_{2.5}
291 emission fractions during evening. The diurnal variations of PM_{2.5} emission from March to May
292 gradually transform from the patterns of winter to those of summer, and *vice versa* for the diurnal
293 variations of PM_{2.5} emission from September to November. The monthly changes of diurnal
294 variations of PM_{2.5} emission are consistent with the seasonal dependence, since monthly variations
295 of PM_{2.5} emission are mainly related to the variations of residential consumptions (Li et al., 2017)
296 in which the space-heating has nearly no diurnal variations and then larger PM_{2.5} emissions during
297 winter lead to reduced diurnal variations than summer. Similar to the monthly fractions of
298 estimated PM_{2.5} emission for mainland China, diurnal variations of PM_{2.5} emission fraction are
299 consistent cross years for a given month (Figure 8). Table 2 gives five-year mean diurnal variations
300 of the estimated PM_{2.5} emission fraction for each month. Based on these high-resolution diurnal-
301 variation fractions, hourly estimates of PM_{2.5} emission can be objectively obtained for a given
302 monthly estimated PM_{2.5} emission.

303 Despite the high temporal resolution, the DEPE also has the ability to analyze diurnal
304 variations for specific cities. The monthly changes of diurnal variations of PM_{2.5} emission
305 estimated for megacities with urban populations larger than 5 million and non-megacities with
306 urban populations smaller than 5 million (Notice of the State Council on Adjusting the Standards
307 for Categorizing City Sizes, 2014) are consistent with those estimated from mainland China
308 (Figure 7). Compared to the diurnal variations of PM_{2.5} emission estimated for mainland China,
309 the megacities have stronger diurnal variations, while the non-megacities have weaker diurnal
310 variations. These detailed descriptions of PM_{2.5} emission that are usually absent in common
311 emission estimates can be essential for PM_{2.5} simulation, especially for providing timely and
312 realistic guidance for severe haze events.

313 There has been lack of local measurements for diurnal variations and widely adopted
314 diurnal variation profiles of $PM_{2.5}$ emission in China. Compared to the diurnal variations of $PM_{2.5}$
315 emission fractions estimated based on diurnal variation profiles from US and EU (Wang et al.,
316 2010; Du et al., 2020), the estimated $PM_{2.5}$ emission fractions are 1.25% larger during the evening, ,
317 which greatly changes the diurnal variations of DEPE. The noon and evening peaks estimated from
318 DEPE have smaller $PM_{2.5}$ emission fractions, with mean underestimations of $PM_{2.5}$ emission
319 fraction of 0.40% and 0.83% for noon peak and evening peak respectively (Figures 7a and 9). In
320 fact, the smaller evening peaks of Wang et al. (2010) occurred in November, December, January,
321 February and March, while they are almost indistinct from April to October, similar to that from
322 DEPE. The morning peak of Wang et al. (2010) is similar to that of DEPE for spring and fall, but
323 the former overestimates $PM_{2.5}$ emission fraction of 0.57% for winter while underestimates $PM_{2.5}$
324 emission fraction of 1.05% for summer. Due to the overestimated peaks, diurnal variations of
325 Wang et al.(2010) have sharper appearance rate for morning peak and disappearance rate for
326 evening peak. Compared to the diurnal variations based on diurnal variation profiles from ES and
327 EU (Wang et al., 2010), the diurnal variations of the DEPE are constrained by the atmospheric-
328 chemical model and observed $PM_{2.5}$ concentrations, which can objectively determine the diurnal
329 variations of $PM_{2.5}$ emission for specific regions and seasons.

330 **5. Impact of COVID-19 on $PM_{2.5}$ emissions**

331 The abrupt outbreak of the COVID-19 pandemic has produced dramatically socioeconomic
332 impacts in China. To prevent the virus spread, a lockdown was first implemented on 23 January
333 2020 in Wuhan, Hubei province, and subsequently the national lockdown has been enforced in
334 China (Liu et al., 2020; Huang et al., 2020; Zhu et al., 2021). Consequently, the total $PM_{2.5}$
335 emission of February 2020 for China shows an obvious decrease compared to those of previous
336 years (Figure 3). The high temporal-resolution DEPE reveals the detailed changes of $PM_{2.5}$
337 emission with time (Figure 10). The $PM_{2.5}$ emission started to decrease right around the COVID
338 outbreak, and had been smaller than those of year 2019 till early March. The emissions at the
339 following months of 2020 are similar to those of 2019, due to the epidemic prevention and control
340 policies enforced by the China government. During February 2020, the DEPE shows significant
341 reductions at the north China plain and northeast of China where prominent $PM_{2.5}$ emission
342 occurred, while spotted $PM_{2.5}$ emission differences with small magnitudes showed at the other

343 regions (Figures 11a-b). Along with recovery from the COVID-19, the estimated PM_{2.5} emission
344 rebounded in March (Figures 3a, 10, 11c-d), which is contributed to the national work resumption.
345 Thus, the DEPE is able to timely reflect the dynamic response of PM_{2.5} emission to the COVID-
346 19.

347 To avoid fluctuations due to diurnal variations and monthly changes of PM_{2.5} emission, 7-
348 day averaged PM_{2.5} emission differences between year 2020 and 2019 are used to analyze the
349 dynamic impact of COVID-19 on PM_{2.5} emission (Figure 12). Before the lockdown, there were
350 slight PM_{2.5} emission differences over several provinces (Figures 12a-b). During the first week of
351 lockdown, PM_{2.5} emission reduction larger than 5×10^{-2} ($\mu\text{g} \cdot \text{m}^{-2} \cdot \text{s}^{-1}$) that is about 60%-70%
352 emission reduction, occurred at Hubei, Hunan, Guangdong, Anhui and Zhejiang provinces (Figure
353 12c). The PM_{2.5} emission reduction extended to BTH and Shandong province during the second
354 week of lockdown (Figure 12d), and continuously spread to the three northeast provinces of China
355 during the third week of lockdown (Figure 12e). During the third week of lockdown, the increased
356 PM_{2.5} emissions for BTH and SCR are possibly caused by the long national vocation of spring
357 holiday of year 2019 (Ji et al., 2018). The inhomogeneous spatial variations of PM_{2.5} emissions
358 possibly relate with different traditions and policy enforcements for different provinces. The PM_{2.5}
359 emission reduction had been maintained over the central and northern China till early March when
360 the lockdown was lift (Figures 12f-i). Though it is hard to see continuous and consistent signal of
361 lockdown for the whole China, the timely DEPE can provide up-to-date guidance for quantifying
362 socioeconomic impacts from rare events with large emission changes such as the COVID-19.

363 Although there were significant reductions of PM_{2.5} emissions over the central and northern
364 China in February 2020, a severe air pollution event occurred over the north China in early
365 February 2020. Previous studies have shown that the factors influencing the severe air pollution
366 event include the still intensive emissions from industrial, power and residential, unfavorable
367 meteorological condition, anomalously high humidity that promoted aerosol heterogeneous
368 chemistry, and secondary aerosol formation associated with increased atmosphere oxidants (Le et
369 al. 2020; Sulaymon et al. 2021; Li et al., 2021) .

370 **6. Discussion**

371 High temporal-resolution and dynamics-based estimations of PM_{2.5} emission can be
372 objectively and optimally obtained by assimilating past and future observed surface PM_{2.5}

373 concentrations through flow-dependent error statistics. This advanced assimilation strategy can be
374 applied for emission estimates of other chemical species when corresponding observations are
375 available, and extend to observation types besides the surface concentrations, like the aerosol
376 optical depth (Liu et al., 2011; Choi et al., 2020). Moreover, current estimates of PM_{2.5} emission
377 are lack of explicitly representations of primary and secondary PM_{2.5}, which could be resolved by
378 joint estimation of the source emission, primary and secondary PM_{2.5} given the concentration
379 observations. Another deficiency of this top-down technique is that it cannot directly determine
380 dynamics-based PM_{2.5} emissions for different sectors and contributions from different policies,
381 although the bottom-up technique has the potential to untangle the different contributions from
382 different policies and quantify the different impacts on different sectors. However, this top-down
383 technique can be integrated into the bottom-up technique to retain advantages of both methods.
384 One future work is to integrate the top-down technique with the bottom-up one, by which the
385 emission estimates for different sectors and polices could be quantified. The annual emission
386 estimate from the bottom-up technique can be further downscaled to hourly estimates by first
387 distributing the annual amount to each month through the monthly allocations estimated from the
388 top-down technique, and then assuming evenly daily distribution, finally applying the fractions of
389 diurnal variation estimated from the top-down technique. The information collected by the bottom-
390 up technique is retained, while the common drawback of coarse temporal resolution for the bottom-
391 up technique is remedied. The integrated bottom-up and top-down technique can improve
392 spatiotemporal representations of source emissions cross time scales and sectors, which is
393 beneficial for emission inventory, air quality forecast, regulation policy and emission trading
394 scheme.

395

396 **Acknowledgments**

397 This work is jointly sponsored by the National Key R&D Program of China through Grant
398 2017YFC1501603 and the National Natural Science Foundation of China through Grants
399 41922036 and 42275153. We are grateful to the High Performance Computing Center of Nanjing
400 University for doing the cycling ensemble assimilation experiments.

401 **Data availability**

402 The meteorological data used for meteorological initial conditions and boundary conditions
403 is available from the University Corporation for Atmospheric Research (UCAR) Research Data
404 Archive (<https://rda.ucar.edu/datasets/ds083.3/>). The assimilated meteorological observations are
405 available from the UCAR Research Data Archive (<https://rda.ucar.edu/datasets/ds337.0/>), and the
406 assimilated chemical observations are available from <https://aqicn.org/map/china/cn/>. The
407 prescribed time-invariant anthropogenic emissions are available from the Emission Database for
408 Global Atmospheric Research for Hemispheric Transport of Air Pollution (EDGAR-HTAP)
409 inventory (https://data.jrc.ec.europa.eu/dataset/jrc-edgar-htap_v2-2) and the Multi-resolution
410 Emission Inventory (MEIC; http://meicmodel.org/?page_id=560).

411 The WRF-Chem model version 3.6.1 is available from
412 https://www2.mmm.ucar.edu/wrf/users/download/get_sources.html#WRF-Chem. The NOAA
413 operational EnKF system is available from [https://dtcenter.org/community-code/gridpoint-](https://dtcenter.org/community-code/gridpoint-statistical-interpolation-gsi)
414 [statistical-interpolation-gsi](https://dtcenter.org/community-code/gridpoint-statistical-interpolation-gsi).

415

416 **Competing interests**

417 The contact author has declared that none of the authors has any competing interests.

418

419 **References**

- 420 Attri, A. K., Kumar, U., and Jain, V. K.: Microclimate: formation of ozone by fireworks, *Nature*, 411, 1015,
421 2001.
- 422 Barker, D., Huang, X.-Y., Liu, Z., Auligné, T., Zhang, X., Rugg, S., Ajjaji, R., Bourgeois, A., Bray, J., Chen,
423 Y., Demirtas, M., Guo, Y.-R., Henderson, T., Huang, W., Lin, H.-C., Michalakes, J., Rizvi, S., and
424 Zhang, X.: The Weather Research and Forecasting Model's Community Variational/Ensemble Data
425 Assimilation System: WRFDA, *B. Am. Meteorol. Soc.*, 93, 831–843, [https://doi.org/10.1175/BAMS-](https://doi.org/10.1175/BAMS-D-11-00167.1)
426 [D-11-00167.1](https://doi.org/10.1175/BAMS-D-11-00167.1), 2012.
- 427 Cao, H., Fu, T.-M., Zhang, L., Henze, D. K., Miller, C. C., Lerot, C., Abad, G. G., De Smedt, I., Zhang, Q., van
428 Roozendaal, M., Hendrick, F., Chance, K., Li, J., Zheng, J., and Zhao, Y.: Adjoint inversion of Chinese
429 non-methane volatile organic compound emissions using space-based observations of formaldehyde
430 and glyoxal, *Atmos. Chem. Phys.*, 18, 15017–15046, <https://doi.org/10.5194/acp-18-15017-2018>, 2018.
- 431 Chen, C., Dubovik, O., Henze, D. K., Chin, M., Lapyonok, T., Schuster, G. L., Ducos, F., Fuertes, D., Litvinov,
432 P., Li, L., Lopatin, A., Hu, Q., and Torres, B.: Constraining global aerosol emissions using

433 POLDER/PARASOL satellite remote sensing observations, *Atmos. Chem. Phys.*, 19, 14585–14606,
434 <https://doi.org/10.5194/acp-19-14585-2019>, 2019.

435 Chin, M., Rood, R. B., Lin, S. J., Muller, J. F., and Thompson, A. M.: Atmospheric sulfur cycle simulated in the
436 global model GO-CART: Model description and global properties, *J. Geophys. Res.-Atmos.*, 105,
437 24671–24687, 2000.

438 Choi, Y., Chen, S. H., Huang, C. C., Earl, K., Chen, C. Y., Schwartz, C. S., and Matsui, T.: Evaluating the impact
439 of assimilating aerosol optical depth observations on dust forecasts over North Africa and the East
440 Atlantic using different data assimilation methods, *Journal of Advances in Modeling Earth Systems*,
441 12(4), e2019MS001890. <https://doi.org/10.1029/2019ms001890>, 2020.

442 Du, Q., Zhao, C., Zhang, M., Dong, X., Chen, Y., Liu, Z., Hu, Z., Zhang, Q., Li, Y., Yuan, R., and Miao, S.:
443 Modeling diurnal variation of surface PM_{2.5} concentrations over East China with WRF-Chem: impacts
444 from boundary-layer mixing and anthropogenic emission, *Atmos. Chem. Phys.*, 20, 2839–2863,
445 <https://doi.org/10.5194/acp-20-2839-2020>, 2020.

446 Elbern, H., Strunk, A., Schmidt, H., and Talagrand, O.: Emission rate and chemical state estimation by 4-dimensional
447 variational inversion, *Atmos. Chem. Phys.*, 7, 3749 – 3769, <https://doi.org/10.5194/acp-7-3749-2007>,
448 2007. Gaspari, G. and Cohn S. E.: Construction of correlation functions in two and three dimensions, *Q.*
449 *J. Roy. Meteor. Soc.*, 125, 723–757, 1999.

450 Ginoux, P., Chin, M., Tegen, I., Prospero, J. M., Holben, B., Dubovik, O., and Lin, S.-J.: Sources and
451 distributions of dust aerosols simulated with the GOCART model, *J. Geophys. Res.*, 106, 20255–20273,
452 doi:10.1029/2000JD000053, 2001.

453 Grell, G., Peckham, S. E., Schmitz, R., McKeen, S. A., Frost, G., Skamarock, W. C., and Eder, B.: Fully coupled
454 “online” chemistry within the WRF model, *Atmos. Environ.*, 39, 6957–6975,
455 <https://doi.org/10.1016/j.atmosenv.2005.04.027>, 2005.

456 Guenther, A., Hewitt, C. N., Erickson, D., Fall, R., Geron, C., Graedel, T., Harley, P., Klinger, L., Lerdau, M.,
457 McKay, W., Pierce, T., Scholes, B., Steinbrecher, R., Tallamraju, R., Taylor, J., and Zimmerman, P.: A
458 global model of natural volatile organic compound emissions, *J. Geophys. Res.*, 100, 8873–8892,
459 doi:10.1029/94JD02950, 1995.

460 Huang, X., Ding, A., Gao, J., Zheng, B., Zhou, D., Qi, X., Tang, R., Wang, J., Ren, C., Nie, W., Chi, X., Xu, Z.,
461 Chen, L., Li, Y., Che, F., Pang, N., Wang, H., Tong, D., Qin, W., Cheng, W., Liu, W., Fu, Q., Liu, B.,
462 Chai, F., Davis, S. J., Zhang, Q., and He, K.: Enhanced secondary pollution offset reduction of primary
463 emissions during COVID-19 lockdown in China, *Natl. Sci. Rev.*, nwa137,
464 <https://doi.org/10.1093/nsr/nwa137>, 2020.

465 Huang, J., Pan, X. C., Guo, X. B., and Li, G. X.: Health impact of China's Air Pollution Prevention and Control
466 Action Plan: an analysis of national air quality monitoring and mortality data, *Lancet Planet. Health*, 2,
467 E313–E323, [https://doi.org/10.1016/S2542-5196\(18\)30141-4](https://doi.org/10.1016/S2542-5196(18)30141-4), 2018.

468 Janssens-Maenhout, G., Crippa, M., Guizzardi, D., Dentener, F., Muntean, M., Pouliot, G., Keating, T., Zhang,
469 Q., Kurokawa, J., Wankmüller, R., Denier van der Gon, H., Kuenen, J. J. P., Klimont, Z., Frost, G.,
470 Darras, S., Koffi, B., and Li, M.: HTAP_v2.2: a mosaic of regional and global emission grid maps for
471 2008 and 2010 to study hemispheric transport of air pollution, *Atmos. Chem. Phys.*, 15, 11411–11432,
472 <https://doi.org/10.5194/acp-15-11411-2015>, 2015.

473 Ji, D., Cui, Y., Li, L., He, J., Wang, L., Zhang, H., Wang, W., Zhou, L., Maenhaut, W., Wen, T., and Wang, Y.:
474 Characterization and source identification of fine particulate matter in urban Beijing during the 2015
475 Spring Festival, *Sci. Total Environ.*, 628–629, 430–
476 440, <https://doi.org/10.1016/j.scitotenv.2018.01.304>, 2018.

477 Jiang, Z., Worden, J. R., Worden, H., Deeter, M., Jones, D. B. A., Arellano, A. F., and Henze, D. K.: A 15-year
478 record of CO emissions constrained by MOPITT CO observations, *Atmos. Chem. Phys.*, 17, 4565–4583,
479 <https://doi.org/10.5194/acp-17-4565-2017>, 2017.

480 Kalnay, E.: *Atmospheric modeling, data assimilation and predictability* (p. 341), Cambridge: Cambridge
481 University Press, 2002.

482 Kleist, D. T., Parrish, D. F., Derber, J. C., Treadon, R., Errico, R. M., and Yang, R.: Improving incremental
483 balance in the GSI 3DVAR analysis system, *Mon. Weather Rev.*, 137, 1046–1060,
484 doi:10.1175/2008MWR2623.1, 2009.

485 Le, T., Wang, Y., Liu, L., Yang, J., Yung, Y. L., Li, G., and Seinfeld, J. H.: Unexpected air pollution with marked
486 emission reductions during the COVID-19 outbreak in China, *Science*, 702–706,
487 <https://doi.org/10.1126/science.abb7431>, 2020.

488 Lei, Y., Zhang, Q., He, K. B., and Streets, D. G.: Primary anthropogenic aerosol emission trends for China,
489 1990–2005, *Atmos. Chem. Phys.*, 11, 931–954, <https://doi.org/10.5194/acp-11-931-2011>, 2011.

490 Li, N., Tang, K., Wang, Y., Wang, J., Feng, W., Zhang, H., Liao, H., Hu, J., Long, X., and Shi, C.: Is the efficacy
491 of satellite-based inversion of SO₂ emission model dependent? *Environmental Research Letters*, 16,
492 035018, 2021.

493 Li, K., Jacob, D. J., Liao, H., Zhu, J., Shah, V., Shen, L., Bates, K. H., Zhang, Q., and Zhai, S.: A Two-Pollutant
494 Strategy for Improving Ozone and Particulate Air Quality in China, *Nat. Geosci.*, 12, 906–
495 910, <https://doi.org/10.1038/s41561-019-0464-x>, 2019a.

496 Li, J. and Wang, Y.: Inferring the anthropogenic NO_x emission trend over the United States during 2003–2017
497 from satellite observations: was there a flattening of the emission trend after the Great Recession? *Atmos.*
498 *Chem. Phys.*, 19, 15339–15352, <https://doi.org/10.5194/acp-19-15339-2019>, 2019b.

499 Li, M., Zhang, Q., Kurokawa, J.-I., Woo, J.-H., He, K., Lu, Z., Ohara, T., Song, Y., Streets, D. G., Carmichael,
500 G. R., Cheng, Y., Hong, C., Huo, H., Jiang, X., Kang, S., Liu, F., Su, H., and Zheng, B.: MIX: a mosaic
501 Asian anthropogenic emission inventory under the international collaboration framework of the MICS-
502 Asia and HTAP, *Atmos. Chem. Phys.*, 17, 935–963, <https://doi.org/10.5194/acp-17-935-2017>, 2017.

503 Li, M., Zhang, Q., Streets, D. G., He, K. B., Cheng, Y. F., Emmons, L. K., Huo, H., Kang, S. C., Lu, Z., Shao,
504 M., Su, H., Yu, X., and Zhang, Y.: Mapping Asian anthropogenic emissions of non-methane volatile
505 organic compounds to multiple chemical mechanisms, *Atmos. Chem. Phys.*, 14, 5617–
506 5638, <https://doi.org/10.5194/acp-14-5617-2014>, 2014.

507 Liu, J., Yin, H., Tang, X., Zhu, T., Zhang, Q., Liu, Z., Tang, X., and Yi, H.: Transition in air pollution, disease
508 burden and health cost in China: A comparative study of long-term and short-term exposure,
509 *Environmental Pollution*, 277, 116770, 2021.

510 Liu, T., Wang, X. Y., Hu, J. L., Wang, Q., An, J. Y., Gong, K. J., Sun, J. J., Li, L., Qin, M. M., Li, J. Y.,
511 Tian, J. J., Huang, Y. W., Liao, H., Zhou, M., Hu, Q. Y., Yan, R. S., Wang, H. L., and Huang, C.:
512 Driving Forces of Changes in Air Quality during the COVID-19 Lockdown Period in the Yangtze River
513 Delta Region, China, *Environ. Sci. Technol.*, 7, 779–786, <https://doi.org/10.1021/acs.estlett.0c00511>,
514 2020.

515 Liu, T., Cai, Y., Feng, B., Cao, G., Lin, H., Xiao, J., Li, X., Liu, S., Pei, L., Fu, L., Yang, X., and Zhang, B.:
516 Long-term mortality benefits of air quality improvement during the twelfth five-year-plan period in 31
517 provincial capital cities of China, *Atmospheric Environment*, 173, 53–61,
518 <https://doi.org/10.1016/j.atmosenv.2017.10.054>, 2018.

519 Liu, Z., Liu, Q., Lin, H. C., Schwartz, C. S., Lee, Y. H., and Wang, T.: Three-dimensional variational
520 assimilation of MODIS aerosol optical depth: implementation and application to a dust storm over
521 East Asia, *J. Geophys. Res.*, 116, D23206, <https://doi.org/10.1029/2011JD016159>, 2011.

522 Miyazaki, K., Bowman, K., Sekiya, T., Eskes, H., Boersma, F., Worden, H., Livesey, N., Payne, V. H., Sudo,
523 K., Kanaya, Y., Takigawa, M., and Ogochi, K.: Updated tropospheric chemistry reanalysis and emission
524 estimates, TCR-2, for 2005–2018, *Earth Syst. Sci. Data*, 12, 2223–2259, [https://doi.org/10.5194/essd-](https://doi.org/10.5194/essd-12-2223-2020)
525 [12-2223-2020](https://doi.org/10.5194/essd-12-2223-2020), 2020.

526 Miyazaki, K., Eskes, H., Sudo, K., Boersma, K. F., Bowman, K., and Kanaya, Y.: Decadal changes in global
527 surface NO_x emissions from multi-constituent satellite data assimilation, *Atmos. Chem. Phys.*, 17, 807–
528 837, <https://doi.org/10.5194/acp-17-807-2017>, 2017.

529 Müller, J.-F., Stavrou, T., Bauwens, M., George, M., Hurtmans, D., Coheur, P.-F., Clerbaux, C., and Sweeney,
530 C.: Top-Down CO Emissions Based on IASI Observations and Hemispheric Constraints on OH Levels,
531 *Geophys. Res. Lett.*, 45, 1621–1629, <https://doi.org/10.1002/2017GL076697>, 2018.

532 Notice of the State Council on Adjusting the Standards for Categorizing City Sizes (in Chinese) (Chinese State
533 Council, 2014); http://www.gov.cn/zwggk/2013-09/12/content_2486773.htm

534 Peng, Z., Lei, L., Liu, Z., Liu, H., Chu, K., and Kou, X.: Impact of Assimilating Meteorological Observations
535 on Source Emissions Estimate and Chemical Simulations, *Geophys. Res. Lett.*, 47,
536 e2020GL089030, <https://doi.org/10.1029/2020GL089030>, 2020.

537 Peng, Z., Lei, L., Liu, Z., Sun, J., Ding, A., Ban, J., Chen, D., Kou, X., and Chu, K.: The impact of multi-species
538 surface chemical observation assimilation on air quality forecasts in China, *Atmos. Chem. Phys.*, 18,
539 17387–17404, <https://doi.org/10.5194/acp-18-17387-2018>, 2018.

540 Peng, Z., Liu, Z., Chen, D., and Ban, J.: Improving PM_{2.5} forecast over China by the joint adjustment of initial
541 conditions and source emissions with an ensemble Kalman filter, *Atmos. Chem. Phys.*, 17, 4837–
542 4855, <https://doi.org/10.5194/acp-17-4837-2017>, 2017.

543 Peng, Z., Zhang, M., Kou, X., Tian, X., and Ma, X.: A regional carbon data assimilation system and its
544 preliminary evaluation in East Asia, *Atmos. Chem. Phys.*, 15, 1087–1104, [https://doi.org/10.5194/acp-](https://doi.org/10.5194/acp-15-1087-2015)
545 [15-1087-2015](https://doi.org/10.5194/acp-15-1087-2015), 2015.

546 Peters, W., Jacobson, A. R., Sweeney, C., Andrews, A. E., Conway, T. J., Masarie, K., Miller, J. B., Bruhwiler,
547 L. M. P., Petron, G., Hirsch, A. I., Worthy, D. E. J., van der Werf, G. R., Randerson, J. T., Wennberg, P.
548 O., Krol, M. C., and Tans, P. P.: An atmospheric perspective on North American carbon dioxide
549 exchange: CarbonTracker, *P. Natl. Acad. Sci. USA*, 104, 18925–18930, 2007.

550 Qu, Z., Henze, D. K., Capps, S. L., Wang, Y., Xu, X., and Wang, J.: Monthly top-down NO_x emissions for
551 China (2005–2012): a hybrid inversion method and trend analysis, *J. Geophys. Res.*, 122, 4600–4625,
552 <https://doi.org/10.1002/2016JD025852>, 2017.

553 Streets, D. G., Bond, T. M. L., Carmichael, G. R., Fernandes, S., Fu, Q., He, D., Klimont, Z., Nelson, S. M.,
554 Tsai, N. Y., Wang, M. Q., Woo, J.-H., and Yarber, K. F.: An inventory of gaseous and primary aerosol
555 emissions in Asia in the year 2000. *J. Geophys. Res.*, 108(D21), 8809, doi:10.1029/2002JD003093,
556 2003.

557 Sulaymon et al. 2021. Persistent high PM_{2.5} pollution driven by unfavorable meteorological conditions during
558 the COVID-19 lockdown period in the Beijing-Tianjin-Hebei region, China. *Environmental*
559 *Research*. <https://doi.org/10.1016/j.envres.2021.111186>

560 Torn, R. D., Hakim, G. J., and Snyder, C.: Boundary conditions for limited-area ensemble Kalman filters, *Mon.*
561 *Weather Rev.*, 134, 2490–2502, 2006.

562 Wang, H., He, X., Liang, X., Choma, E. F., Liu, Y., Shan, L., Zheng, H., Zhang, S., Nielsen, C. P., Wang, S.,
563 Wu, Y., and Evans, J. S.: Health benefits of on-road transportation pollution control programs in China,
564 *P. Natl. Acad. Sci. USA*, 117, 25370, <https://doi.org/10.1073/pnas.1921271117>, 2020.

565 Wang, G., Cheng, S. Y., Wei, W., Yang, X. W., Wang, X. Q. Jia, J., Lang, J. L., and Lv, Z.: Characteristics and
566 emission reduction measures evaluation of PM_{2.5} during the two major events: APEC and Parade, *Sci.*
567 *Total Environ.*, 595, 81–92, <https://doi.org/10.1016/j.scitotenv.2017.03.231>, 2017.

568 Wang, Z., Li, J., Wang, Z., Yang, W., Tang, X., Ge, B., Yan, P., Zhu, L., Chen, X., and Chen, H.: Modeling study
569 of regional severe hazes over mid-eastern China in January 2013 and its implications on pollution
570 prevention and control, *Sci. China-Earth Sci.*, 57, 3–13, 2014.

571 Wang, X. Y., Liang, X. Z., Jiang, W. M., Tao, Z. N., Wang, J. X. L., Liu, H. N., Han, Z. W., Liu, S. Y., Zhang, Y. Y.,
572 Grell, G. A., and Peckham, S. E.: WRF-Chem simulation of East Asian air quality: Sensitivity to temporal
573 and vertical emissions distributions, *Atmos. Environ.*, 44, 660–669, 2010.

574 Whitaker, J. S. and Hamill, T. M.: Ensemble data assimilation without perturbed observations, *Mon. Weather Rev.*,
575 130, 1913–1924, 2002.

576 Whitaker, J. S. and Hamill, T. M.: Evaluating methods to account for system errors in ensemble data assimilation,
577 *Mon. Weather Rev.*, 140, 3078–3089, 2012.

578 Yang, Y., Ren, L., Li, H., Wang, H., Wang, P., Chen, L., Yue, X., and Liao, H.: Fast climate responses to aerosol
579 emission reductions during the COVID-19 pandemic, *Geophys. Res. Lett.*, 47,
580 e2020GL089788, <https://doi.org/10.1029/2020gl089788>, 2020.

581 Zhai, S., Jacob, D. J., Wang, X., Liu, Z., Wen, T., Shah, V., Li, K., Moch, J. M., Bates, K. H., Song, S., Shen,
582 L., Zhang, Y., Luo, G., Yu, F., Sun, Y., Wang, L., Qi, M., Tao, J., Gui, K., Xu, H., Zhang, Q., Zhao, T.,
583 Wang, Y., Lee, H. C., Choi, H., and Liao, H.: Control of particulate nitrate air pollution in China, *Nat.*
584 *Geosci.*, 14, 1–7, 2021.

585 Zhang, Q., Zheng, Y., Tong, D., Shao, M., Wang, S., Zhang, Y., Xu, X., Wang, J., He, H., Liu, W., Ding, Y.,
586 Lei, Y., Li, J., Wang, Z., Zhang, X., Wang, Y., Cheng, J., Liu, Y., Shi, Q., Yan, L., Geng, G., Hong, C.,
587 Li, M., Liu, F., Zheng, B., Cao, J., Ding, A., Gao, J., Fu, Q., Huo, J., Liu, B., Liu, Z., Yang, F., He, K.,
588 and Hao, J.: Drivers of Improved PM_{2.5} Air Quality in China from 2013 to 2017, *P. Natl. Acad. Sci.*
589 *USA*, 116, 24463–24469, <https://doi.org/10.1073/pnas.1907956116>, 2019.

590 Zhang, L., Shao, J. Y., Lu, X., Zhao, Y. H., Hu, Y. Y., Henze, D. K., Liao, H., Gong, S., and Zhang, Q.: Sources
591 and processes affect-ing fine particulate matter pollution over North China: An adjoint analysis of the
592 Beijing APEC period, *Environ. Sci. Technol.*, 50, 8731–8740, <https://doi.org/10.1021/acs.est.6b03010>,
593 2016.

594 Zhang, Q., Streets, D. G., Carmichael, G. R., He, K. B., Huo, H., Kannari, A., Klimont, Z., Park, I. S., Reddy,
595 S., Fu, J. S., Chen, D., Duan, L., Lei, Y., Wang, L. T., and Yao, Z. L.: Asian emis- sions in 2006 for the
596 NASA INTEX-B mission, *Atmos. Chem. Phys.*, 9, 5131–5153, [https://doi.org/10.5194/acp-9-5131-](https://doi.org/10.5194/acp-9-5131-2009)
597 2009, 2009.

598 Zheng, B., Zhang, Q., Geng, G., Chen, C., Shi, Q., Cui, M., Lei, Y., and He, K.: Changes in China's
599 anthropogenic emissions and air quality during the COVID-19 pandemic in 2020, *Earth Syst. Sci. Data*,
600 13, 2895–2907, <https://doi.org/10.5194/essd-13-2895-2021>, 2021.

601 Zheng, B., Geng, G., Ciais, P., Davis, S. J., Martin, R. V., Meng, J., Wu, N., Chevallier, F., Broquet, G., Boersma,
602 F., van der A, R., Lin, J., Guan, D., Lei, Y., He, K., and Zhang, Q.: Satellite-based estimates of decline
603 and rebound in China's CO₂ emissions during COVID-19 pandemic, *Sci. Adv.*, 6,
604 eabd4998, <https://doi.org/10.1126/sciadv.abd4998>, 2020.

605 Zheng, B., Tong, D., Li, M., Liu, F., Hong, C., Geng, G., Li, H., Li, X., Peng, L., Qi, J., Yan, L., Zhang, Y.,
606 Zhao, H., Zheng, Y., He, K., and Zhang, Q.: Trends in China's anthropogenic emissions since 2010 as

607 the consequence of clean air actions, *Atmos. Chem. Phys.*, 18, 14095–14111,
608 <https://doi.org/10.5194/acp-18-14095-2018>, 2018.
609 Zhu, J., Chen, L., Liao, H., Yang, H., Yang, Y., and Yue, X.: Enhanced PM_{2.5} Decreases and O₃ Increases in
610 China during COVID-19 Lockdown by Aerosol-Radiation Feedback, *Geophys. Res. Lett.*, 48,
611 e2020GL090260, <https://doi.org/10.1029/2020GL090260>, 2021.

612
613

614 **Figures and Tables**

615 **Captions:**

616 **Figure 1.** Times series of hourly PM_{2.5} concentration biases ($\mu\text{g}\cdot\text{m}^{-3}$). The ensemble mean priors
617 compared to the observed quantities for December of years 2016-2020 (gray and black), and the
618 mean biases of years 2016-2020 (blue).

619 **Figure 2.** Model domain and observation sites for cycling assimilation. Red and blue dots denote
620 the assimilated and unassimilated observational sites, respectively.

621 **Figure 3.** (a) Dynamics-based monthly PM_{2.5} emission estimates ($\text{Tg}\cdot\text{day}^{-1}$) summed over
622 mainland China of each year from 2016 to 2020 (colored) and the estimated PM_{2.5} emission from
623 MEIC (gray); (b) Ratio of PM_{2.5} emission changes between two adjacent years from year 2016 to
624 2020 normalized by the PM_{2.5} emission of year 2016; (c) Monthly fractions of dynamics-based
625 PM_{2.5} emission estimates for years 2016-2020 (light blue), the five-year mean fractions of
626 dynamics-based monthly PM_{2.5} emission estimates with bars denoting one standard deviation of
627 the five-year variations (dark blue), and the monthly fractions of estimated PM_{2.5} emission from
628 MEIC (gray).

629 **Figure 4.** (a) Spatial distribution of dynamics-based PM_{2.5} emission estimates ($\mu\text{g}\cdot\text{m}^{-2}\cdot\text{s}^{-1}$) for
630 year 2016, and compared to that of year 2016, spatial distributions of dynamics-based PM_{2.5}
631 emission changes of year (b) 2017, (c) 2018, (d) 2019 and (e) 2020.

632 **Figure 5.** (a) The differences of dynamics-based PM_{2.5} emission estimates between years 2017-
633 2020 and 2016, and (b) the differences normalized by that of year 2016.

634 **Figure 6.** Spatial distributions of dynamics-based PM_{2.5} emission changes in December compared to November
635 in (a) 2017 and (b) 2018.**Figure 7.** Five-year mean diurnal variations of dynamics-based PM_{2.5}
636 emission fraction averaged over (a) mainland China, (b) megacities with urban population ≥ 5
637 million, and (c) non-megacities with urban population < 5 million.

638 **Figure 8.** Diurnal variations of dynamics-based PM_{2.5} emission fractions for years 2016-2020
639 (light blue) and five-year mean fractions with bars denoting one standard deviation of the five-
640 year variations (dark blue) are averaged over mainland China for (a) January, (b) April, (c) July,
641 and (d) October.

642 **Figure 9.** Diurnal variations of PM_{2.5} emission fraction for each month based on diurnal variation
643 profiles from ES and EU (Wang et al. 2010).

644 **Figure 10.** Hourly (light red and blue) and daily (dark red and blue) dynamics-based PM_{2.5}
645 emission estimates (kg·h⁻¹) summed over mainland China from January to March of years 2019
646 and 2020.

647 **Figure 11.** Spatial distributions of dynamics-based PM_{2.5} emission estimates (μg·m⁻²·s⁻¹) on (b)
648 February and (d) March of year 2019, and spatial distributions of dynamics-based PM_{2.5} emission
649 reduction of year 2020 compared to year 2019 for (c) February and (e) March.

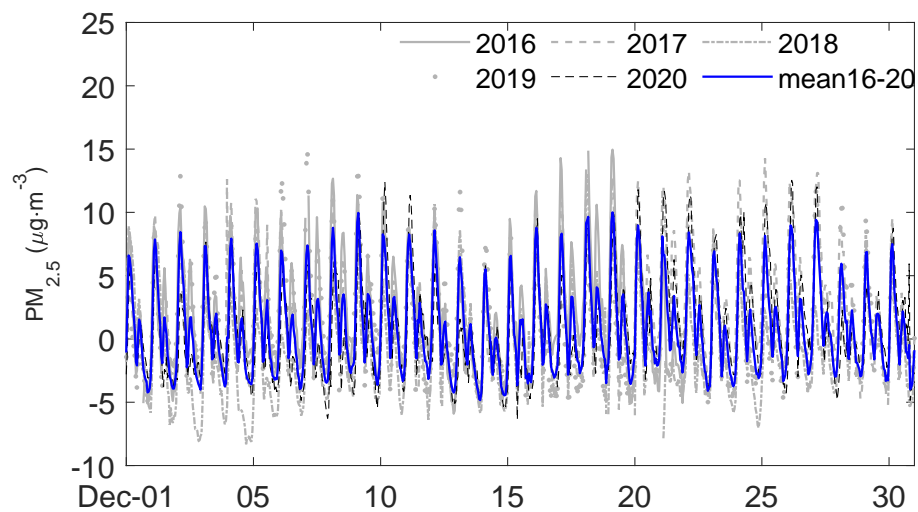
650 **Figure 12.** Mean spatial distributions of PM_{2.5} emission differences (μg·m⁻²·s⁻¹) between year
651 2020 and 2019 for 9 weeks starting at 9 January 2020. Negative (positive) values indicate that
652 PM_{2.5} emission of year 2020 is smaller (larger) than that of year 2019. The numbers in (a) denote
653 provinces as: 1 Heilongjiang, 2 Neimenggu, 3 Xinjiang, 4 Jilin, 5 Liaoning, 6 Gansu, 7 Hebei, 8
654 Beijing, 9 Shanxi, 10 Tianjin, 11 Shanxi, 12 Ningxia, 13 Qinghai, 14 Shandong, 15 Xizang, 16
655 Henan, 17 Jiangsu, 18 Anhui, 19 Sichuan, 20 Hubei, 21 Chongqing, 22 Shanghai, 23 Zhejiang, 24
656 Hunan, 25 Jiangxi, 26 Yunnan, 27 Guizhou, 28 Fujian, 29 Guangxi, 30 Guangdong, 31 Taiwan,
657 32 Hongkong, 33 Macao, 34 Hainan.

658 **Table 1.** Dynamics-based PM_{2.5} emission estimates of year 2016 for each province whose value
659 is larger than 0.01 μg·m⁻²·s⁻¹ are shown in the second column. Ratios of PM_{2.5} emission changes
660 of years 2017-2020 compared to year 2016 are shown from the third to the sixth column, with
661 negative (positive) values indicating decrease (increase) of PM_{2.5} emission.

662 **Table 2.** Five-year mean diurnal fractions (%) of the dynamics-based PM_{2.5} emission estimates
663 over mainland China on local solar time (LST) for each month.

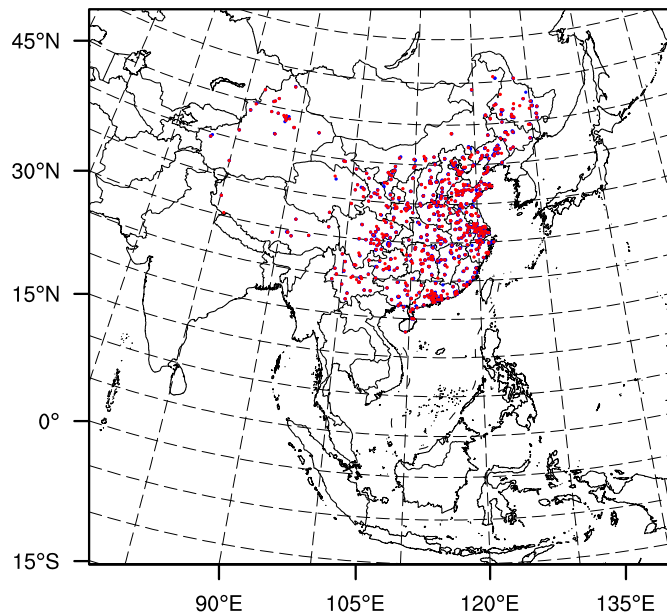
664

665
666



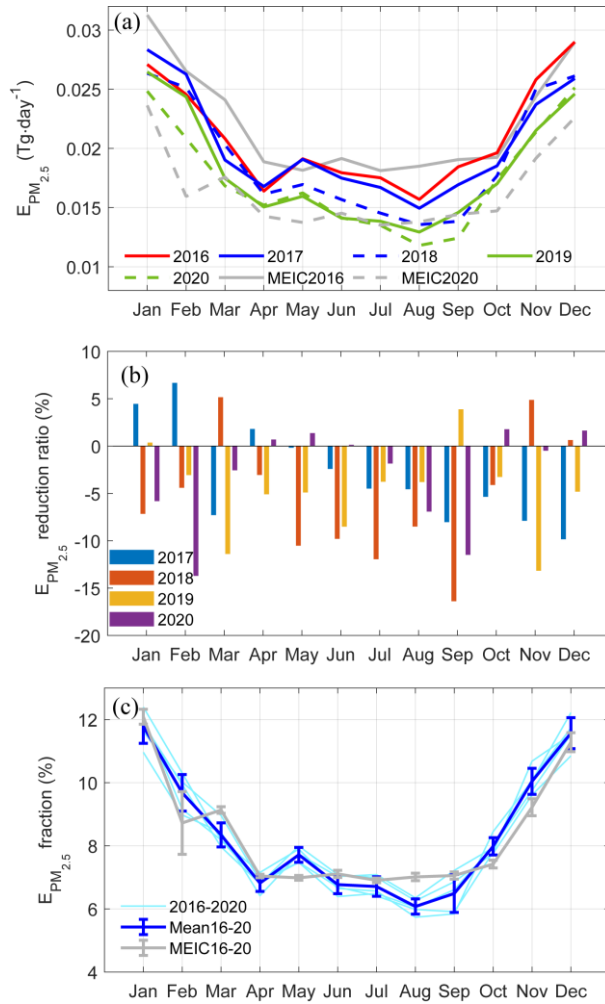
667
668
669
670
671
672
673

Figure 1. Times series of hourly PM_{2.5} concentration biases (μg·m⁻³). The ensemble mean priors compared to the observed quantities for December of years 2016-2020 (gray and black), and the mean biases of years 2016-2020 (blue).

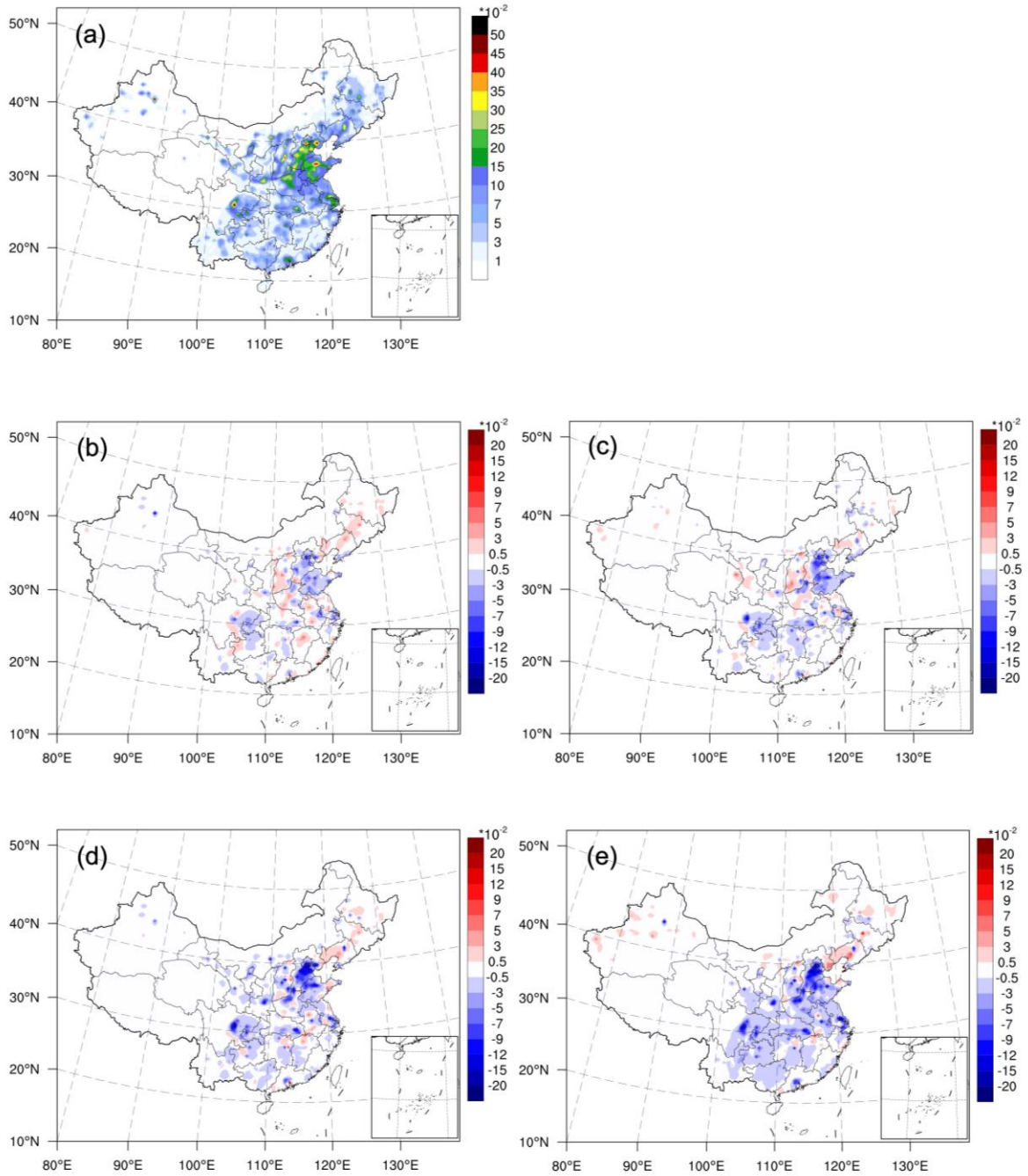


675
676
677
678
679

Figure 2. Model domain and observation sites for cycling assimilation. Red and blue dots denote the assimilated and unassimilated observational sites, respectively.



680
 681 **Figure 3.** (a) Dynamics-based monthly PM_{2.5} emission estimates (Tg·day⁻¹) summed over mainland China of
 682 each year from 2016 to 2020 (colored) and the estimated PM_{2.5} emission from MEIC (gray); (b) Ratio of PM_{2.5}
 683 emission changes between two adjacent years from year 2016 to 2020 normalized by the PM_{2.5} emission of
 684 year 2016; (c) Monthly fractions of dynamics-based PM_{2.5} emission estimates for years 2016-2020 (light blue),
 685 the five-year mean fractions of dynamics-based monthly PM_{2.5} emission estimates with bars denoting one
 686 standard deviation of the five-year variations (dark blue), and the monthly fractions of estimated PM_{2.5}
 687 emission from MEIC (gray).
 688
 689
 690
 691
 692
 693



694
 695
 696
 697
 698
 699
 700
 701

Figure 4. (a) Spatial distribution of dynamics-based PM_{2.5} emission estimates ($\mu\text{g}\cdot\text{m}^{-2}\cdot\text{s}^{-1}$) for year 2016, and compared to that of year 2016, spatial distributions of dynamics-based PM_{2.5} emission changes of year (b) 2017, (c) 2018, (d) 2019 and (e) 2020.

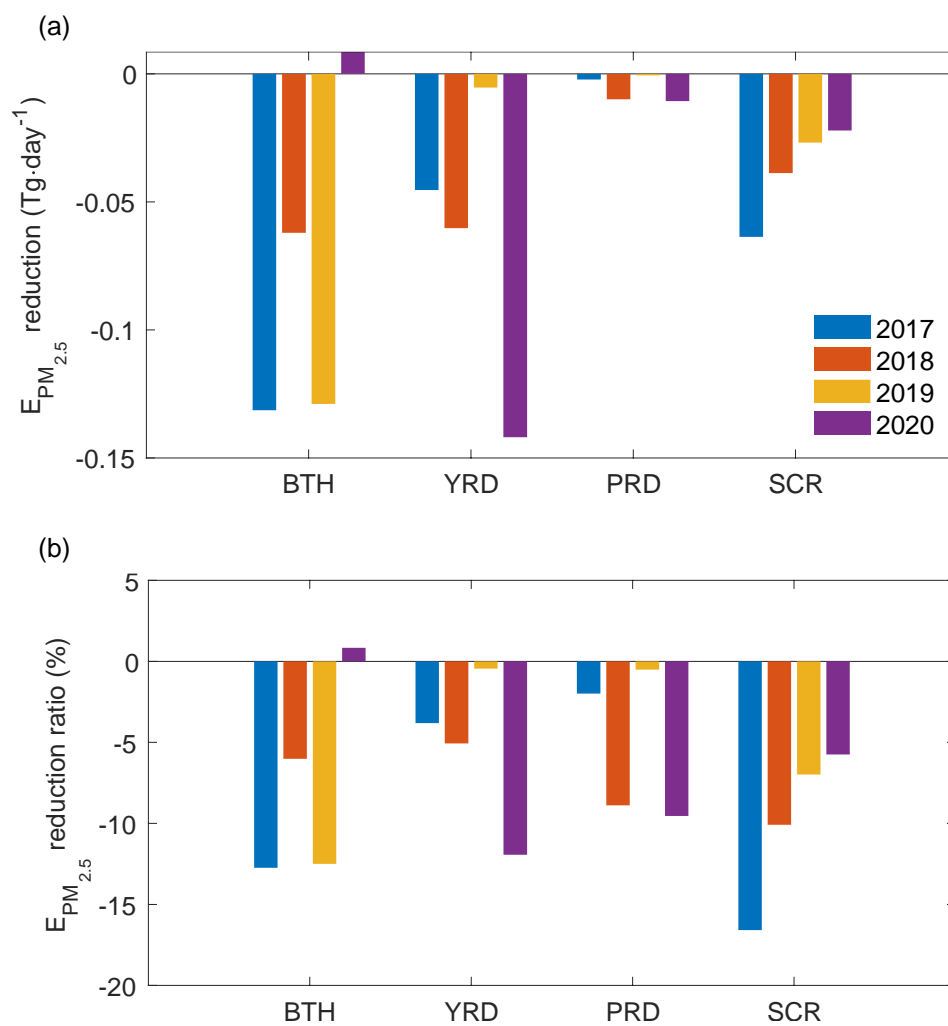


Figure 5. (a) The differences of dynamics-based PM_{2.5} emission estimates between years 2017-2020 and 2016, and (b) the differences normalized by that of year 2016.

703
704
705
706
707

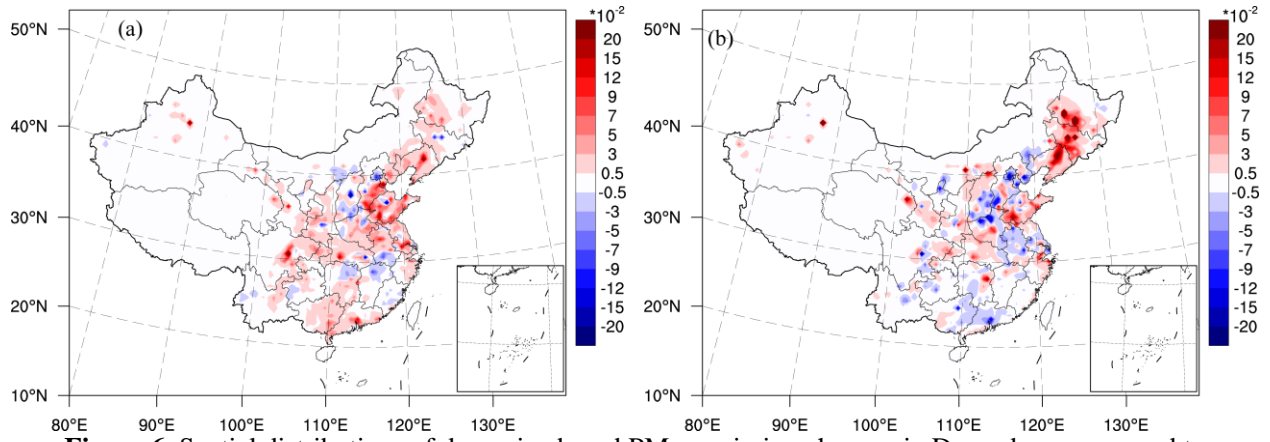
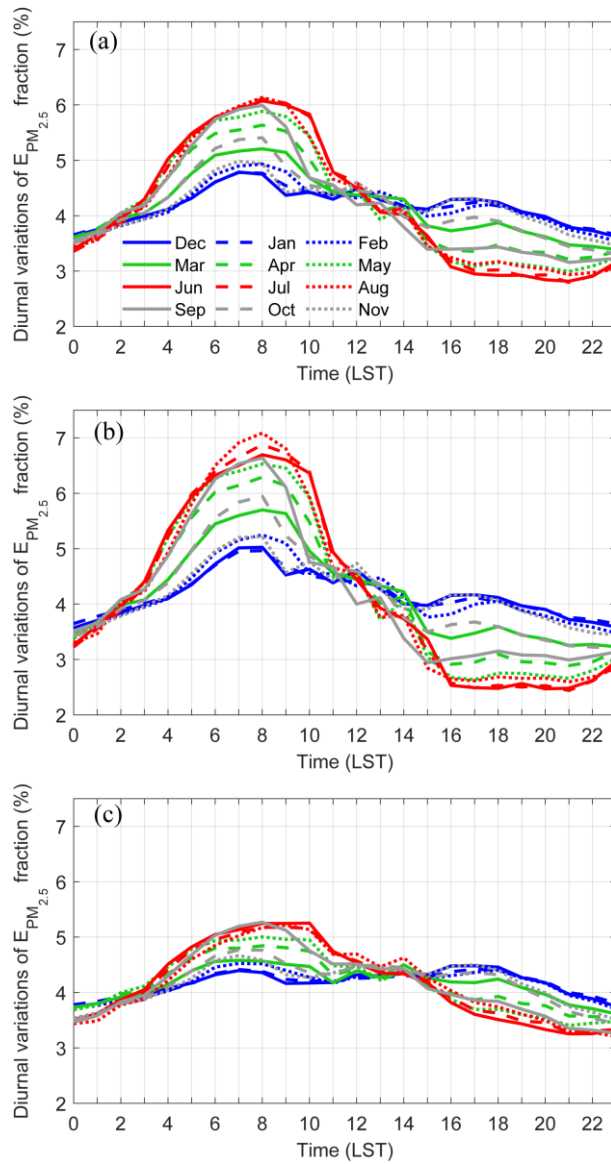


Figure 6. Spatial distributions of dynamics-based PM_{2.5} emission changes in December compared to November in (a) 2017 and (b) 2018.

708
709
710
711

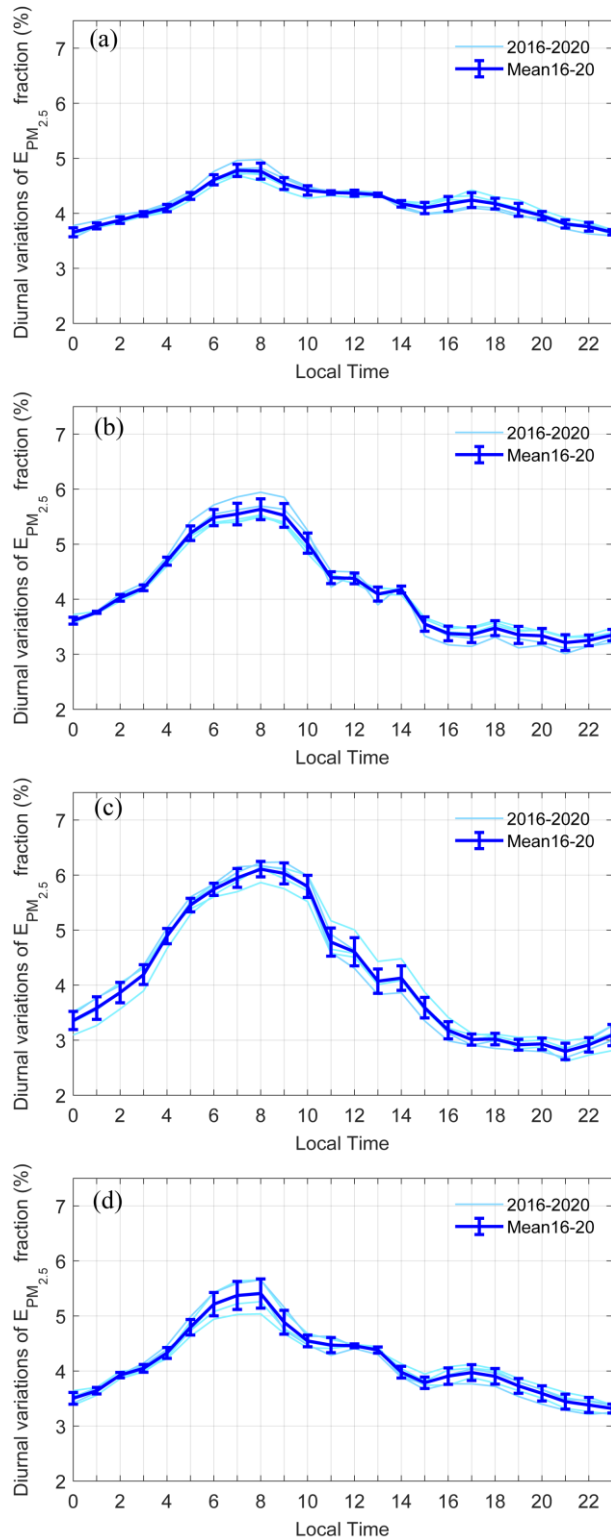


712

713 **Figure 7.** Five-year mean diurnal variations of dynamics-based $PM_{2.5}$ emission fraction averaged over (a) mainland

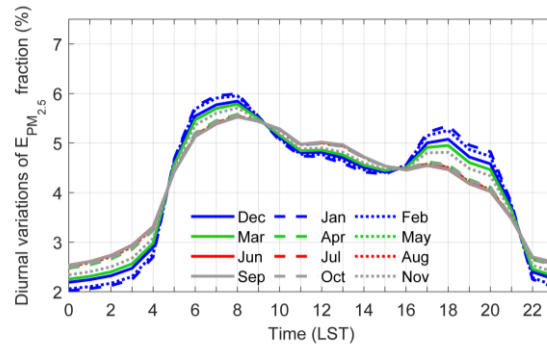
714 China, (b) megacities with urban population ≥ 5 million, and (c) non-megacities with urban population < 5 million.

715



716
 717 **Figure 8.** Diurnal variations of dynamics-based PM_{2.5} emission fractions for years 2016-2020
 718 (light blue) and five-year mean fractions with bars denoting one standard deviation of the five-
 719 year variations (dark blue) are averaged over mainland China for (a) January, (b) April, (c) July,
 720 and (d) October.
 721

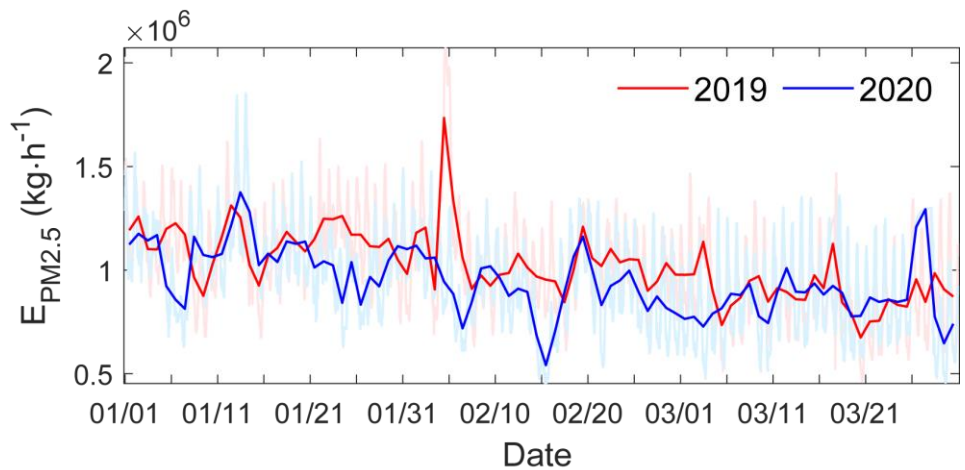
722
723
724



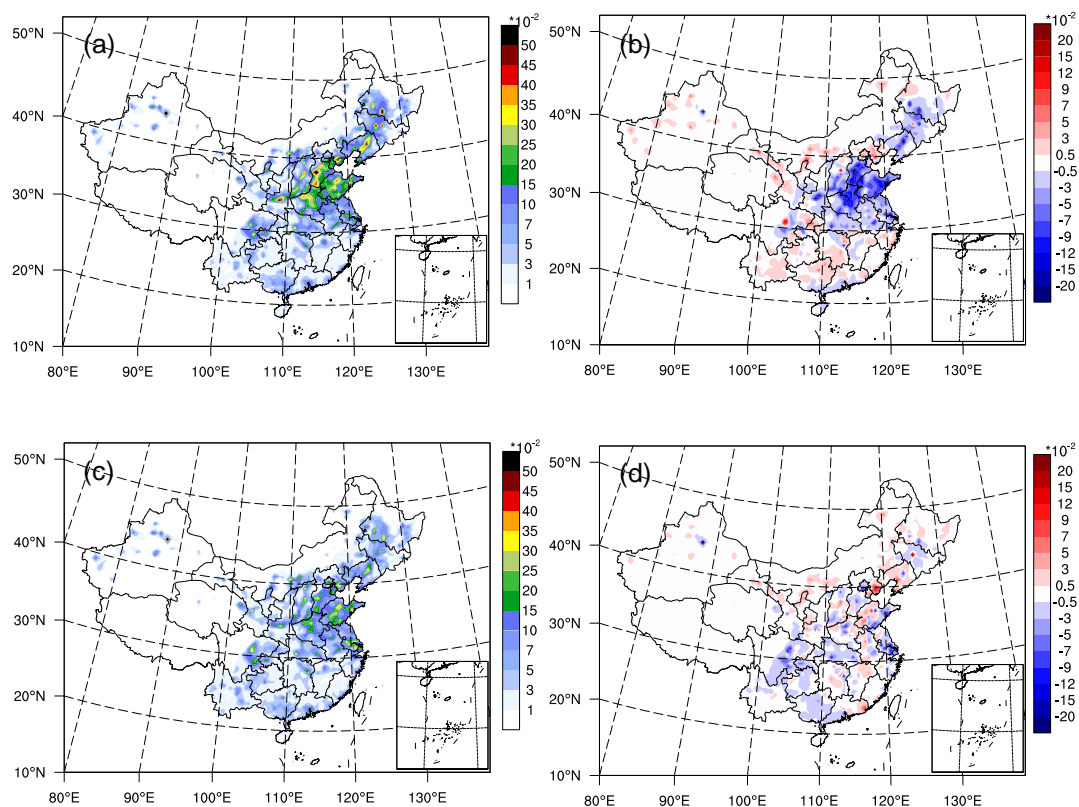
725
726
727
728

Figure 9. Diurnal variations of PM_{2.5} emission fraction for each month based on diurnal variation profiles from ES and EU (Wang et al. 2010).

729
730
731



732
733 **Figure 10.** Hourly (light red and blue) and daily (dark red and blue) dynamics-based PM_{2.5} emission estimates ($\text{kg} \cdot \text{h}^{-1}$)
734 summed over mainland China from January to March of years 2019 and 2020.
735



737

738

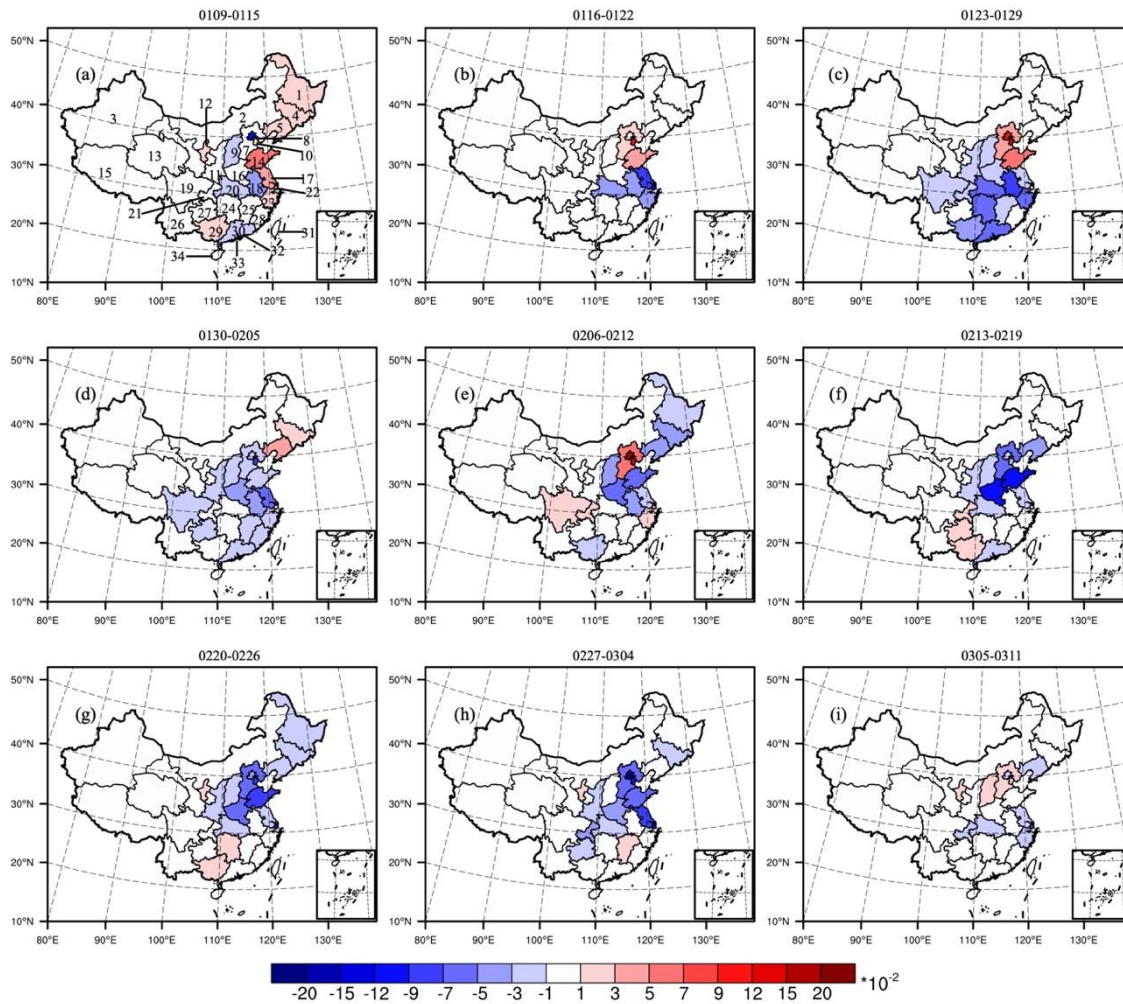
739

740

741

742

Figure 11. Spatial distributions of dynamics-based PM_{2.5} emission estimates ($\mu\text{g}\cdot\text{m}^{-2}\cdot\text{s}^{-1}$) on (b) February and (d) March of year 2019, and spatial distributions of dynamics-based PM_{2.5} emission reduction of year 2020 compared to year 2019 for (c) February and (e) March.



744 **Figure 12.** Mean spatial distributions of PM_{2.5} emission differences ($\mu\text{g}\cdot\text{m}^{-2}\cdot\text{s}^{-1}$) between year
 745 2020 and 2019 for 9 weeks starting at 9 January 2020. Negative (positive) values indicate that
 746 PM_{2.5} emission of year 2020 is smaller (larger) than that of year 2019. The numbers in (a) denote
 747 provinces as: 1 Heilongjiang, 2 Neimenggu, 3 Xinjiang, 4 Jilin, 5 Liaoning, 6 Gansu, 7 Hebei, 8
 748 Beijing, 9 Shanxi, 10 Tianjin, 11 Shanxi, 12 Ningxia, 13 Qinghai, 14 Shandong, 15 Xizang, 16
 749 Henan, 17 Jiangsu, 18 Anhui, 19 Sichuan, 20 Hubei, 21 Chongqing, 22 Shanghai, 23 Zhejiang,
 750 24 Hunan, 25 Jiangxi, 26 Yunnan, 27 Guizhou, 28 Fujian, 29 Guangxi, 30 Guangdong, 31
 751 Taiwan, 32 Hongkong, 33 Macao, 34 Hainan.

752

753

754 **Table 1.** Dynamics-based PM_{2.5} emission estimates of year 2016 for each province whose value
 755 is larger than 0.01 μg·m⁻²·s⁻¹ are shown in the second column. Ratios of PM_{2.5} emission changes
 756 of years 2017-2020 compared to year 2016 are shown from the third to the sixth column, with
 757 negative (positive) values indicating decrease (increase) of PM_{2.5} emission.
 758

Province	PM _{2.5} emission of year 2016 (μg·m ⁻² ·s ⁻¹)	Percentage of PM _{2.5} emission change for year 2017 (%)	Percentage of PM _{2.5} emission change for year 2018 (%)	Percentage of PM _{2.5} emission change for year 2019 (%)	Percentage of PM _{2.5} emission change for year 2020 (%)
Tianjin	0.2083	-14.07	-22.99	-38.70	-26.98
Shanghai	0.2067	-24.39	-30.21	-21.46	-30.05
Shandong	0.1631	-15.26	-21.02	-15.57	-19.41
Beijing	0.1598	-26.64	-25.75	-41.92	-45.27
Hebei	0.1178	-7.47	-11.98	-26.39	-22.87
Jiangsu	0.1088	-6.52	-3.98	-12.69	-28.20
Henan	0.1064	-1.41	-3.68	-12.15	-24.91
Shanxi	0.0885	<u>6.17</u>	<u>7.90</u>	-13.18	-13.85
Liaoning	0.0742	<u>6.32</u>	-2.58	<u>3.22</u>	<u>11.42</u>
Anhui	0.0687	<u>1.92</u>	-5.63	-6.23	-21.57
Hubei	0.0574	-5.87	-17.69	-19.76	-36.48
Zhejiang	0.0557	-3.62	-9.32	-9.99	-18.05
Chongqing	0.0525	-22.24	-29.81	-24.63	-38.41
Shanxi	0.0498	<u>0.62</u>	-1.97	-18.05	-17.85
Guangdong	0.0481	<u>1.21</u>	-6.01	-6.69	-14.37
Ningxia	0.0481	-8.17	-5.93	-24.46	-12.95
Hunan	0.0417	-6.40	-19.35	-9.91	-20.62
Guangxi	0.0390	-2.42	-3.52	-12.47	-22.31
Guizhou	0.0365	-4.01	-15.82	-21.74	-46.41
Jilin	0.0360	<u>12.30</u>	-3.22	<u>7.37</u>	<u>4.76</u>
Jiangxi	0.0353	<u>13.22</u>	-9.67	-7.19	-11.91
Sichuan	0.0337	-7.66	-15.66	-27.68	-37.93
Fujian	0.0244	<u>3.13</u>	-2.73	-8.13	-13.41
Heilongjiang	0.0231	<u>7.30</u>	-0.21	<u>3.14</u>	<u>3.91</u>
Yunnan	0.0221	-1.26	-7.16	-9.93	-15.35
Gansu	0.0177	-4.26	<u>5.28</u>	-17.89	-16.49
Hainan	0.0173	<u>3.93</u>	-0.41	-5.04	-4.78
Neimenggu	0.0141	-0.00	-3.63	-8.16	<u>3.55</u>

759
760

761 **Table 2.** Five-year mean diurnal fractions (%) of the dynamics-based PM_{2.5} emission estimates
 762 over mainland China on local solar time (LST) for each month.

	Jan	Feb	Mar	Apr	May	Jun	Jul	Aug	Sep	Oct	Nov	Dec
0	3.65	3.58	3.61	3.61	3.55	3.40	3.36	3.44	3.55	3.50	3.53	3.63
1	3.77	3.69	3.72	3.76	3.74	3.65	3.58	3.56	3.70	3.64	3.64	3.75
2	3.88	3.82	3.96	4.03	4.05	3.94	3.86	4.01	4.05	3.93	3.83	3.89
3	3.98	3.94	4.05	4.21	4.29	4.30	4.19	4.14	4.19	4.05	3.93	3.99
4	4.10	4.06	4.33	4.69	4.92	5.03	4.89	4.71	4.69	4.33	4.12	4.12
5	4.32	4.38	4.76	5.20	5.46	5.48	5.45	5.39	5.27	4.80	4.45	4.32
6	4.61	4.74	5.09	5.48	5.72	5.78	5.74	5.78	5.74	5.21	4.83	4.61
7	4.78	4.90	5.17	5.55	5.78	5.92	5.95	5.98	5.92	5.37	4.98	4.79
8	4.77	4.93	5.21	5.63	5.88	6.07	6.11	6.13	5.99	5.41	4.94	4.75
9	4.54	4.79	5.14	5.52	5.79	6.00	6.03	6.02	5.60	4.89	4.42	4.37
10	4.41	4.41	4.68	5.02	5.43	5.83	5.79	5.42	4.68	4.55	4.50	4.42
11	4.38	4.40	4.42	4.39	4.45	4.79	4.78	4.66	4.56	4.47	4.36	4.30
12	4.37	4.32	4.37	4.38	4.48	4.49	4.61	4.51	4.19	4.46	4.60	4.48
13	4.34	4.43	4.34	4.09	3.93	4.06	4.07	4.09	4.23	4.38	4.33	4.29
14	4.17	4.26	4.30	4.18	4.16	4.02	4.13	4.10	3.79	3.98	4.10	4.15
15	4.10	3.99	3.82	3.55	3.46	3.63	3.59	3.45	3.39	3.79	4.07	4.12
16	4.17	4.05	3.73	3.38	3.17	3.08	3.18	3.24	3.40	3.92	4.30	4.29
17	4.24	4.17	3.79	3.36	3.08	2.95	3.01	3.12	3.41	3.98	4.31	4.30
18	4.18	4.21	3.87	3.48	3.16	2.92	3.03	3.17	3.44	3.91	4.21	4.24
19	4.06	4.04	3.72	3.35	3.12	2.92	2.93	3.08	3.34	3.73	3.99	4.07
20	3.96	3.93	3.62	3.34	3.07	2.84	2.93	3.04	3.29	3.59	3.85	3.98
21	3.81	3.75	3.47	3.21	2.99	2.83	2.80	2.93	3.16	3.44	3.65	3.79
22	3.76	3.66	3.44	3.25	3.09	2.91	2.92	2.97	3.19	3.38	3.56	3.73
23	3.65	3.55	3.39	3.34	3.23	3.16	3.09	3.04	3.23	3.32	3.47	3.62

763

764

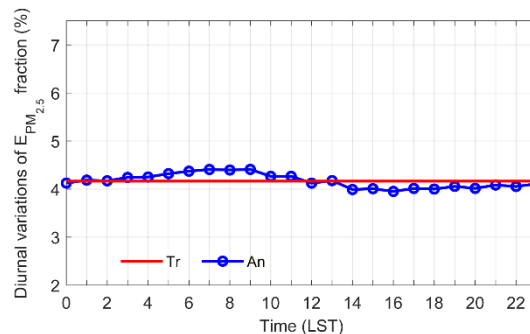
765

766

767 **Appendix: Effects of meteorology**

768 An observing system simulation experiment (OSSE) is performed to investigate the effects of time-
769 varying boundary layer. A nature run is first conducted from 0000 UTC 25 December 2015 to
770 0000 UTC 2 February 2016, forced by the time-invariant source emissions PR2010 (the true
771 emission). Synthetic observations of the six conventional air pollutant concentrations (i.e., PM₁₀,
772 PM_{2.5}, SO₂, NO₂, O₃, and CO) are generated from the natural run. Hourly synthetic observations
773 are created from 0000 UTC 29 December 2015 to 0006 UTC 1 February 2016, by interpolating
774 the gridded true surface concentrations to the chemical observation locations with additive random
775 errors of $N(0, R)$. R is the observation error variance, which is calculated by the formula in Elbern
776 et al. (2007). Outputs from the first four days of the natural run are excluded to avoid the transient
777 effect. Then the prior emissions are generated by $F^{pr} = (1.8 + \delta(x, y, z, t))F^{tr}$, where F^{tr} is the true
778 emission, δ is a random number sampled from the normal distribution $N(0,1)$ (Peng et al. 2015).
779 Ensemble data assimilation experiments are conducted from 0000 UTC 29 December to 0006 UTC
780 1 February 2016. Outputs from the first two days of the OSSE are excluded due to the spin-up.

781 The magnitude of posterior PM_{2.5} emission is closer to the true emission than the prior. Figure S1
782 presents the monthly mean diurnal variations of PM_{2.5} emission fraction from the OSSE. It shows
783 that a little larger estimated PM_{2.5} emission fractions occurred in the morning and smaller
784 estimated PM_{2.5} emission fractions occurred in the afternoon, comparing to the time-invariant true
785 emission. But the diurnal variations of PM_{2.5} emission fractions caused by the boundary layer are
786 not as strong as that caused by the emission itself (Figure 7). The reason may be that we have
787 hourly assimilated observations to simultaneously update the chemical concentrations and source
788 emissions. Therefore, the impacts of time-varying boundary layer on the posterior PM_{2.5} emissions
789 are limited.



790

791 **Figure S1.** Diurnal variations of PM_{2.5} emission fraction for the Observing System Simulation
792 Experiment.